Influence of a Hydroxyl Group on the Deamidation and Dehydration Reactions of Protonated Asparagine-Serine Investigated by Combined Spectroscopic, Guided Ion Beam, and Theoretical Approaches

Georgia C. Boles,[1] Lisanne J. M. Kempkes,[2] Jonathan Martens,[2] Giel Berden,[2] Jos Oomens,[2,3,*] P. B. Armentrout[1,*]

[1] Department of Chemistry, University of Utah, 315 S. 1400 E. Rm. 2020, Salt Lake City, Utah 84112, USA

[2] Radboud University, Institute for Molecules and Materials, FELIX Laboratory, Toernooiveld 7, 6525 ED, Nijmegen, The Netherlands

[3] Van't Hoff Institute for Molecular Sciences, University of Amsterdam, Science Park 904, 1098 XH Amsterdam, The Netherlands

* Corresponding authors: JO: j.oomens@science.ru.nl; PBA: armentrout@chem.utah.edu

Abstract: Deamidation of asparaginyl (Asn) peptides is a spontaneous post-translational modification that plays a significant role in degenerative diseases and other biological processes under physiological conditions. In the gas phase, deamidation of protonated peptides is a major fragmentation channel upon activation by collision-induced dissociation. Here, we present a full description of the deamidation process from protonated asparagine-serine, $[AsnSer+H]^+$, via infrared (IR) action spectroscopy and threshold collision-induced dissociation (TCID) experiments in combination with theoretical calculations. The IR results demonstrate that deamidation proceeds via bifurcating reaction pathways leading to furanone and succinimide type product ion structures, with a population analysis indicating the latter product dominates. Theory demonstrates that nucleophilic attack of the peptidyl amide oxygen onto the Asn side chain leads to furanone formation, whereas nucleophilic attack by the peptidyl amide nitrogen onto the Asn side-chain carbonyl carbon leads to the formation of the succinimide product structure. TCID experiments find that furanone formation has a threshold energy of 145 ± 12 kJ/mol and succinimide formation occurs with a threshold energy of 131 ± 12 kJ/mol, consistent with theoretical energies and with

the spectroscopic results indicating that succinimide dominates. The results provide information regarding the inductive and steric effects of the Ser side chain on the deamidation process. The other major channel observed in the TCID experiments of $[AsnSer+H]^+$ is dehydration, where a threshold energy of 104 ± 10 kJ/mol is determined. A complete IR and theoretical analysis of this pathway is also provided. As for deamidation, a bifurcating pathway is found with both dominant oxazoline and minor diketopiperazine products identified. Here, the Ser side chain is directly involved in both pathways.

Introduction

Under physiological conditions, deamidation of the asparagine (Asn) residues of proteins (leading to the formation of a succinimide intermediate upon expulsion of ammonia)[1-2] is a spontaneously occurring post-translational modification. Generally, the succinimide is rapidly hydrated to form both aspartyl and iso-aspartyl residues, with the latter formed preferentially. Overall, the effects of this process include altered protein function,[3-4] reduced vaccine efficiency,[5] detrimental protein aging,[6-8] and protein folding disorders,[6, 9-11] largely resulting from the iso-aspartyl residue. Therefore, considerable effort has been expended in distinguishing the isobaric aspartyl and iso-aspartyl residues using mass spectrometry.[12-13]

Deamidation rates are known to depend on the solution pH and are enhanced in alkaline solutions.[14] Intriguingly, the deamidation rates of several peptides are strongly influenced by the neighboring C-terminal residue.[15] Specifically, deamidation half-times of GlyYyyAsnXxxGly pentapeptides, where Xxx = glycine (Gly), serine (Ser), alanine (Ala), threonine (Thr), and valine (Val), were found to be 1.2, 16, 25, 47, and 253 days, respectively,[15] as averages for all Yyy (any of the 20 natural amino acids). Explanations for the range in deamidation rates were associated mainly with steric effects of the Xxx residue, although no detailed mechanistic or structural analyses were completed. Therefore, in the current work, we establish the likely mechanisms for possible deamidation processes of protonated AsnSer ($[AsnSer+H]^+$), identify the deamidation product(s) formed, and evaluate the reaction threshold for deamidation via infrared (IR) action

spectroscopy and threshold collision-induced dissociation (TCID) experiments, coupled with theory. This work complements analogous studies conducted previously on $[AsnXxx+H]^+$ for Xxx = Gly,[16] Ala,[17-18] Val,[19] and Thr.[20]

Succinimide intermediate formation as a result of Asn deamidation is well-documented in the literature;[1-2, 21] however, given the intrinsic differences between a dipeptide and a protein as well as between gas-phase and condensed-phase reactivity, we have also explored alternative pathways that may exist for ammonia loss. As shown in Scheme 1, the reactions shown in green (Succinimide formation, Suc) and pink (furanone formation, Fur) present two likely deamidation pathways via nucleophilic attack driven dissociations. In each reaction, collisional activation allows migration of the proton to the side-chain nitrogen atom, thereby allowing neutral ammonia (NH_3) to be expelled from the Asn side chain, inducing deamidation. For succinimide formation, the peptidyl amide nitrogen acts as the nucleophile attacking the side-chain amide carbon leading to a 5-membered Suc ring structure. The alternative nucleophilic attack of the peptidyl amide oxygen on the side-chain amide carbon yields a 5-membered Fur ring structure. Given in blue, we also considered a deamination pathway for ammonia loss from the backbone, which leads to the formation of a 6-membered diketo-morpholine (DKM) ring structure by nucleophilic attack of the C-terminal oxygen on the α-carbon of the first residue.

As noted above, the deamidation processes of protonated AsnXxx dipeptides with Xxx = Gly,[16] Ala,[17-18] Val,[19] and Thr[20] *n + 1* residues have been previously evaluated using the same methods employed here. Deamidation of $[AsnGly+H]^+$ leads to a Suc structure at threshold energies, with contribution from the Fur product at higher collision energies.[16] The deamidation of $[AsnAla+H]^+$ proceeds along bifurcating pathways resulting in the observation of both Fur and Suc structures,[17-18] whereas the deamidation of $[AsnVal+H]^+$ results exclusively in the formation of a Fur structure.[19] In contrast, the deamidation of $[AsnThr+H]^+$ leads predominantly to the formation of a Suc product ion,[20] with a minor contribution of Fur. Thus, the current results, compared with our previous analyses of $[AsnGly+H]^+$, $[AsnAla+H]^+$, $[AsnVal+H]^+$, and

$[AsnThr+H]^+$ should allow for the determination of C-terminal residue side-chain effects with respect to both size and side-chain functionality.

The other major decomposition product observed in the present study results from dehydration. In a recent paper,[22] the dehydration product ions formed from several protonated dipeptides containing side chains with hydroxyl groups (AlaSer, AlaThr, GlySer, GlyThr, PheSer, PheThr, ProSer, ProThr, AsnSer and AsnThr) were examined using IR action spectroscopy coupled with quantum-chemical calculations. In all cases, including AsnSer, the results unambiguously show that dehydration produces oxazoline structures $[OxaI+H]^+$, rather than the oxazolone $[OxaO+H]^+$ expected for dehydration at the C-terminus. For AsnSer, there was also evidence for a second structure, suggested in the previous work to probably be the thermodynamically favored monoketopiperazine $[MKP+H]^+$ product, which is formed by H_2O expulsion from the Ser side chain via attack by the N-terminal amino nitrogen. Here, we provide a detailed reaction mechanism for the pathway yielding the oxazoline product and we reexamine which isomer might be the second structure because several additional structures for the dehydration products were located in the interim.

Experimental and Computational Methods

IRMPD Spectroscopy. Infrared multiple-photon dissociation (IRMPD) spectra of $[AsnSer+H]^+$, $[AsnSer+H\text{-}NH_3]^+$, and $[AsnSer+H\text{-}H_2O]^+$ were measured using infrared radiation produced by the free-electron laser FELIX.[23] The IR laser beam is coupled into a modified 3D quadrupole ion trap mass spectrometer (Bruker, AmaZon Speed ETD, Bremen, Germany)[24] via a KRS-5 window on the vacuum housing and a 3-mm diameter hole in the ring electrode of the ion trap. The protonated precursor dipeptide was generated via electrospray ionization (ESI) from an approximately 10 μM solution of the dipeptide (Biomatik, Canada) in 50/50 MeOH/H_2O with ~1% formic acid added to enhance protonation. This solution was infused at a flow rate of 120 μL/hr. The $[AsnSer+H]^+$ precursor ion (*m/z* 220) was isolated. Collisional activation of the protonated

precursor ions could be effected using helium as the background gas for approximately 40 ms and an amplitude parameter of ~0.3 V, adjusting the activation parameters to optimize the formation of either $[AsnSer+H–NH_3]^+$ or $[AsnSer+H-H_2O]^+$ ions at *m/z* 203 and 202, respectively. IRMPD spectra were then recorded for the isolated parent and product ions over the 800 – 2000 cm^{-1} frequency range. Ions were irradiated with two 6-μs long macropulses from FELIX at a repetition rate of 10 Hz, each having a pulse energy of approximately 60 mJ, with energies gradually dropping to about 20 mJ towards the high frequency end of the scan range. The bandwidth of the FELIX radiation was about 0.5% of the center frequency. The extent of dissociation at each wavelength is expressed as the dissociation yield via $yield = \sum I(fragment)/[I(precursor) + \sum I(fragment)]$, where I is the ion intensity determined from five averaged mass spectra. The yield was corrected for variations in the pulse energy over the scan range assuming a linear power dependence of the fragmentation signal.

Guided Ion Beam Mass Spectrometry. Kinetic energy dependent cross sections for the CID of $[AsnSer+H]^+$ with Xe were measured using a guided ion beam tandem mass spectrometer (GIBMS) (U. of Utah) that has been described in detail elsewhere.[25-27] Ions were generated using an electrospray ionization (ESI) source[28] under similar conditions to those described previously. The ESI was operated using 5×10^{-5} M AsnSer in 50/50 MeOH/H_2O solution, acidified with acetic acid, and syringe-pumped at a rate of 50 μL/hr into a 35 gauge stainless steel needle biased at 2000 – 3000 V relative to ground. Ions were directed through a heated capillary at 80 °C into a radio frequency (rf) ion funnel,[29] where they were focused into a tight beam. After exiting the ion funnel, the ions entered a rf trapping hexapole ion guide where they underwent on the order of 10^4 thermalizing collisions with ambient gas. As demonstrated in earlier studies, ions produced in the source region should have a Maxwell-Boltzmann distribution of rovibrational states at 300 K.[28, 30-32]

Precursor ions were extracted from the source, mass selected using a magnetic momentum analyzer, decelerated to a well-defined kinetic energy, and focused into a rf octopole ion guide that traps the ions radially,[33] which minimizes losses of product and reactant ions. The octopole passes

through a collision cell containing xenon[34] at pressures < 0.3 mTorr. The product and residual reactant ions drifted to the end of the octopole guide, where they were extracted and focused into a quadrupole mass filter for mass analysis. Ions were detected with a high voltage dynode and scintillation detector,[35] and the signal was processed using standard pulse counting techniques.

Ion intensities of reactants and products, measured as a function of collision energy, were converted to absolute cross sections as described previously.[25] Briefly, calculation of the total cross section (σ_{tot}) from the ion intensities utilizes a relationship that is directly analogous to the Beer-Lambert Law, specifically, $I = I_0 \, exp(-\rho\sigma_{tot}l)$, where I is the reactant ion intensity after passing through the collision cell, I_0 is the reactant ion intensity entering the collision cell which equals $I + \sum I_j$ (where I_j = intensity of the product ion for channel j), l is the effective length of the collision cell (8.3 cm), and ρ is the number density of the neutral reactant and equals P/k_BT, where P and T are the pressure and temperature of the gas and k_B is Boltzmann's constant. Reaction cross sections for individual product ions are given by $\sigma_j = \sigma_{tot} \, (I_j / \sum I_j)$. The uncertainty in these relative cross sections is about ±5% and that for the absolute cross sections is about ±20%. The ion kinetic energy distribution was measured using a retarding potential analysis and found to be Gaussian with a typical full width at half maximum (FWHM) of 0.1 - 0.2 eV (lab). Ion kinetic energies in the laboratory (lab) frame were converted to energies in the center-of-mass (CM) frame using $E_{CM} = E_{lab} \, m/(m + M)$, where M and m are the masses of the ionic and neutral reactants, respectively. Uncertainties in the absolute energy scale are about ±0.05 eV (lab), which translates to ±0.02 eV (CM) here. All energies below are reported in the CM frame.

Thermochemical Analysis. Thresholds of TCID cross sections for fragmentation channel j were modeled using eq 1,

$$\sigma_j(E) = (n\sigma_0/E) \sum_i g_i \int_{E_{0,j-Ei}}^{E} \left[k_j(E^*)/k_{tot}(E^*)\right] \left\{1 - e^{-k_{tot}(E^*)\tau}\right\} (E - \varepsilon)^{n-1} d(\varepsilon) \quad (1)$$

where σ_0 is an energy-independent scaling factor, n is an adjustable, empirical representation of factors that describe the efficiency of the energy transfer during collision and varies with the complexity of the system being studied,[26] E is the relative kinetic energy of the reactants, $E_{0,j}$ is the

threshold for dissociation of the ground electronic and rovibrational state of the reactant ion into channel j at 0 K, τ is the experimental time for dissociation (~5 x 10^{-4} s, as measured by previous time-of-flight studies[26]), ε is the energy transferred from translation to internal modes during the collision, and E^* is the internal energy of the energized molecule (EM) after the collision, so that $E^* = \varepsilon + E_i$. The summation is over the rovibrational states of the reactant ions, i, where E_i is the excitation energy of each state and g_i is the fractional population of those states ($\Sigma g_i = 1$). The Beyer–Swinehart-Stein-Rabinovitch algorithm[36-37] was used to evaluate the number and density of the rovibrational states and the relative populations g_i were calculated for a Maxwell-Boltzmann distribution at 300 K. The term $k_j(E^*)$ is the unimolecular rate constant for dissociation of the EM to channel j via its rate-limiting transition state (TS). The rate constants $k_j(E^*)$ and $k_{tot}(E^*)$ were defined by Rice-Ramsperger-Kassel-Marcus (RRKM) theory as in eq 2,[38-39]

$$k_{tot}(E^*) = \sum_j k_j(E^*) = \sum_j s_j N_j^{\dagger}(E^* - E_{0,j})/h\rho(E^*) \qquad (2)$$

where s_j is the reaction degeneracy of channel j, $N_j^{\dagger}(E^* - E_{0,j})$ is the sum of rovibrational states for the TS of channel j at an energy $E^* - E_{0,j}$, h is Planck's constant, and $\rho(E^*)$ is the density of states of the EM at the available energy, E^*. These rate constants allow both kinetic shifts (where the probability of dissociation is given by the term $P_D = [1 - e^{-k_{tot}(E^*)\tau}]$ in eq 1) and competition between multiple channels (which is controlled by the ratio of rate constants in eq 1, $[k_j(E^*)/k_{tot}(E^*)]$) to be modeled accurately.[40-41]

Several effects complicate the data analysis and must be accounted for to produce accurate thermodynamic information. First, the kinetic energy distributions of the reactants result in energy broadening, which is accounted for by explicit convolution of the model over kinetic energy distributions of both reactants, as described elsewhere.[25, 42] After this convolution, the threshold model of eq 1 includes all sources of energy available to the reactants. Second, cross sections must correspond to single-collision events in order for the energy deposition to be accurately modeled using eq 1. To ensure single collision conditions, data obtained under high mass resolution conditions were collected at three pressures of Xe, here about 0.3, 0.2, and 0.1 mTorr, and the

resulting cross sections evaluated for pressure effects and extrapolated to zero pressure when pressure effects outside the range of experimental error were detected. Third, eq 1 accounts for the average lifetime for dissociation, which can result in a kinetic shift of the CID threshold and increases as the size of the molecule increases, as well as competition between channels.[40-41]

To evaluate the rate constants in eqs 1 and 2, the needed sets of rovibrational frequencies for the EM and rate-limiting TSs were determined from quantum chemical calculations discussed in the following section. The model cross sections of eq 1 were convoluted with the kinetic energy distributions of the reactants[25] and compared to the experimental data. A nonlinear least-squares analysis was used to provide optimized values for σ_0, n, and $E_{0,j}$. The uncertainty in $E_{0,j}$ (one standard deviation) was estimated from the range of threshold values determined from multiple sets of data, variations in the parameter n (±10% around the optimum value), variations in vibrational frequencies (±10%), changes in τ by factors of 2, and the uncertainty in the absolute energy scale (0.02 eV). The entropy of activation at 1000 K for each dissociation channel was calculated as described in detail elsewhere.[40-41]

Computational Chemistry. Quantum-chemical calculations were used to optimize molecular geometries and to predict IR spectra for isomeric fragment ion structures that were deemed possible by chemical intuition, including all likely protomers. First, guessed structures were optimized at the density functional theory (DFT) level with the B3LYP/6-31++G(d,p) basis set, using Gaussian 09 revision D01.[43] For the lowest-energy structures of the $[AsnSer+H]^+$, $[AsnSer+H–NH_3]^+$, and $[AsnSer+H–H_2O]^+$ fragments, the potential energy surfaces were further explored to identify the lowest-energy conformers using a molecular mechanics/molecular dynamics (MM/MD) approach employing AMBER 12. After minimization within AMBER, a simulated annealing procedure up to 500 K was used. Five hundred structures were obtained by this procedure and grouped based on structural similarity using appropriate rms criteria to give 20 – 30 candidate structures. Next, these structures were each optimized using DFT at the B3LYP/6-311+G(d,p) level. For the purpose of comparison with experimental spectra, the DFT computed harmonic vibrational frequencies were scaled by 0.975 (which accounts for inaccuracies in the

calculated values, anharmonic effects on the absorption, as well as the multiphoton character of the absorption) and convoluted with a 20 cm^{-1} full-width-at half-maximum Gaussian line shape.

Regarding structures located along key reaction coordinates, structures (low-energy conformers and additional key reaction intermediates and transition states) previously reported for $[AsnThr+H]^+$ [20] were used as starting structures, where a hydrogen replaced the methyl group of the Thr side chain. Optimizations of all unique low-energy structures were conducted at the B3LYP/6-311+G(d,p) level of theory. Each TS was verified to contain one imaginary frequency, and it was determined that each intermediate/product structure was vibrationally stable.

Rotational constants and vibrational frequencies were calculated from structures optimized at the B3LYP/6-311+G(d,p) level. In order to account for inaccuracies in the calculated vibrational frequencies, as detailed elsewhere,[44] they were scaled by a factor of 0.989 when used for the determination of internal energy, RRKM calculations, zero-point vibrational energy (ZPE) corrections, and thermal corrections from 0 K to 298 K. Single point energies of all species were calculated using the 6-311+G(2d,2p) basis set at the B3LYP, B3P86, and MP2(full) levels (where full indicates correlation of all electrons) using the B3LYP/6-311+G(d,p) geometries.

Results and Discussion

Precursor Ion: [AsnSer+H]$^+$. Similar to $[AsnGly+H]^+$, $[AsnAla+H]^+$, $[AsnVal+H]^+$, and $[AsnThr+H]^+$,[16-20] different levels of theory predict different $[AsnSer+H]^+$ ground structures (GSs) at 0 K, Figure 1 (where the last structure gives an overview of the nomenclature used to identify the $[AsnSer+H]^+$ heteroatoms). Notably, all low-energy conformers protonate at the amino nitrogen (N^1), and the protonation site participates in hydrogen bonding to the carbonyl oxygens of the peptide bond ($N^1H\bullet O^1C$) as well as of the Asn side chain ($N^1H\bullet O^{s1}C$). Similar to the $[AsnThr+H]^+$ system,[20] each of the low-energy conformers also exhibits a hydrogen bond between the peptide bond and the hydroxyl oxygen of the side chain ($N^2H\bullet O^{s2}$). The B3LYP functional predicts $[AsnSer+H]^+$-1 to be the GS, whereas MP2 predicts $[AsnSer+H]^+$-2 to be ~3 kJ/mol lower in energy at 0 K. These two structures are nearly isoenergetic at the B3P86 level of theory. The

latter structure adopts a head-to-tail configuration via a hydrogen bond between the amide Asn side chain and the C-terminal carbonyl oxygen ($N^sH\bullet O^2C$). The two structures interconvert by a dihedral angle rotation of 120° with a transition state (imaginary frequency = 57 cm^{-1}) calculated to lie 8 – 16 kJ/mol above $[AsnSer+H]^+$-1. A third low-lying structure, $[AsnSer+H]^+$-3, adopts similar H-bonding as structure 1 with different dihedral angles along the backbone. This conformer lies 11 – 16 kJ/mol above structure 1 at 0 K. All levels of theory suggest that the $[AsnSer+H]^+$-1 species is the lowest energy structure at 298 K, with the 2 isomer lying 5.6, 3.8, and 1.2 kJ/mol higher at the B3LYP, B3P86, and MP2 levels, respectively. Thus, a 298 K equilibrium distribution of the 1:2 isomers would have populations of 91:9%, 82:18%, and 62:38%, respectively.

IRMPD Spectrum of $[AsnSer+H]^+$. Figure 1 also shows the IRMPD spectrum of the precursor ion compared with theoretical spectra predicted at the B3LYP/6-311+G(d,p) level. Major spectral features in the experimental spectrum are centered at 1774, 1714, 1607, 1526, 1404, 1146, and 1086 cm^{-1}, which agree well with the spectrum predicted for the 298 K GS, $[AsnSer+H]^+$-1. The calculated spectrum for this structure predicts bands at 1769 (carboxylic acid CO stretch); 1709 (peptide bond amide CO stretch) and 1683 (Asn side-chain amide CO stretch); 1616, 1607, and 1585 (primarily amine NH_3 motions); 1514 (peptide bond NH wag); 1411 (NH_3 umbrella); 1148 (carboxylic acid COH bend); and 1086, 1077, and 1070 (delocalized motions along the peptide chain) cm^{-1}. As discussed above, $[AsnSer+H]^+$-3 adopts a similar structure such that similarly characterized bands at 1781, 1709, 1685, 1616, 1512, 1399, 1143, and 1059 cm^{-1} are predicted for this species (Figure 1). Note that the band at 1059 cm^{-1} does not reproduce experiment as well as the 1070 – 1086 cm^{-1} bands of $[AsnSer+H]^+$-1, and its relatively high energy suggests that the $[AsnSer+H]^+$-3 species is not formed experimentally. Likewise, the predicted spectrum for $[AsnSer+H]^+$-2 does not reproduce the experimental spectrum well, indicating that this species is not appreciably formed experimentally. However, the small band observed at 1475 cm^{-1} (not found in $[AsnSer+H]^+$-1) could indicate a non-negligible population of this structure, consistent with its low relative energy. We conclude that $[AsnSer+H]^+$-1 is the dominant contributor to the spectrum, with a minor contribution from $[AsnSer+H]^+$-2.

TCID Cross Sections. Experimental kinetic energy dependent cross sections were measured for the interaction of Xe and $[AsnSer+H]^+$, *m/z* 220, under unit mass resolution conditions, as discussed previously.[16, 18] A representative data set measured at 0.2 mTorr of Xe is given in Figure 2, and eight product channels were measured. An overview of these pathways is indicated in Scheme 2, which depicts the likely or lowest-energy pathways found for these decomposition processes. Notably, not all of these product structures were confirmed by spectroscopic means and therefore those for the more minor channels are speculative. The dominant dissociation channels observed, with apparent energy onsets of ~0.9 and 1.2 eV, are measured at *m/z* 202 and 203 and correspond to loss of water and ammonia, respectively. As demonstrated below, deamidation leads to both protonated furanone, $[Fur+H]^+$, and succinimide structures, $[Suc+H]^+$. Several pathways were explored for dehydration and IR spectroscopic results reported elsewhere[22] (and reviewed below) indicate the primary formation of a protonated oxazoline, $[OxaI+H]^+$, structure.

At nearly 1 eV higher in energy, *m/z* 87 (loss of Ser + CO leading to formation of protonated 3-iminopropanamide, $NH_2C(=O)CH_2CH=NH_2^+$, $[IPA+H]^+$) and 106 (formation of $[Ser+H]^+$ + OACP, 1-oxa-3,5-amino-cyclopentan-2-one) channels are observed. On the basis of the IRMPD results discussed below, it is also likely that the dehydration product (*m/z* 202) dissociates to yield $[IPA+H]^+$ + 4-carboxylic acid-2-oxazoline (CAOxaI) and its complement, IPA + $[CAOxaI+H]^+$ (*m/z* 116), which appears at higher energies. At comparable high energies, *m/z* 161 and 186 are observed. On the basis of the IRMPD results presented below, *m/z* 186 is identified as sequential loss of ammonia from the primary deamidation product (*m/z* 203) and the *m/z* 161 channel is believed to correspond to ketene loss from the deamidation product forming $[GlySer-H]^+$. At the highest energies studied, the production of *m/z* 133 is observed with a small intensity, possibly $[Asn+H]^+$ formed by loss of $C_3H_5NO_2$ (dehydrated serine). Other fragments observed at high energies include *m/z* 185 (sequential loss of NH_3 and H_2O from $[AsnSer+H]^+$, which IRMPD results indicate can occur in either order), 157 (loss of CO from *m/z* 185) , and 140

(likely loss of NH_3 from *m/z* 157), but their intensities were smaller than the ions included in Figure 2.

Structures of the Deamidation Product Ion, [AsnSer+H-NH₃]⁺. Many possible deamidation products were explored computationally, as shown in Table 1. Relative single point energies for the possible $[Suc+H]^+$, $[Fur+H]^+$, and $[DKM+H]^+$ products outlined in Scheme 1 are given for various protonation sites at the B3LYP and MP2 levels of theory. At the B3LYP level of theory, $[DKM+H]^+$-2, protonated at the carboxamide oxygen O^{s1} (see Scheme 1), is predicted to be the $[AsnSer+H-NH_3]^+$ GS at both 0 and 298 K. All other $[DKM+H]^+$ structures are at least 66 kJ/mol higher in energy. Despite this low energy, comparison between the experimental IRMPD spectrum and calculated spectra for low-energy DKM structures, given in the Supporting Information, Figure S1, suggest this species is not formed experimentally. Therefore, our focus was primarily on $[Suc+H]^+$ and $[Fur+H]^+$ formation. At the B3LYP level of theory, $[Suc+H]^+$-4 (protonation at O^{s1}, Scheme 1) has the lowest energy of these species, whereas the MP2 level of theory indicates that $[Suc+H]^+$-1 (protonation at N^1) is the overall lowest energy $[AsnSer+H-NH_3]^+$ structure. Both levels of theory agree that there are low-lying structures for both sites, and also for protonation at the other ring carbonyl (O^1, site 2), which lies above the lowest-energy $[Suc+H]^+$ structure by 8 – 20 kJ/mol. In contrast, protonation at the carboxylic acid carbonyl (O^2, site 5) is higher by 48 – 68, and protonation at N^2 (site 3) is more than 116 kJ/mol higher. The lowest-energy $[Fur+H]^+$ structures are protonated at N^2 ($[Fur+H]^+$-3, Scheme 1) and lie 15 – 41 kJ/mol above the lowest energy $[Suc+H]^+$ species. Proton migration to other sites in $[Fur+H]^+$ results in energies considerably higher (>70 kJ/mol), Table 1.

Given these results, conformers of $[Suc+H]^+$-1, 2, and 4 along with $[Fur+H]^+$-3 were computationally located, and their relative energies are provided in Table 2. The three lowest energy structures of each of these species are shown in Figure 3 and select higher-energy structures are given in Figure S2. For **$[Suc+H]^+$-1.y**, the conformers differ primarily in the hydrogen bonding orientation of the N^1 protonation site. **$[Suc+H]^+$-1.1**, the 0 K GS at the MP2 level, orients the Ser backbone such that both $N^1H\bullet O^2C$ and $O^{s2}H\bullet O^{s1}C$ hydrogen bonds are formed, whereas **$[Suc+H]^+$-**

1.2, the 298 K GS at the MP2 level, rotates the Ser side chain away to break the latter interaction, and **1.3** instead forms a hydrogen bond between the protonated N^1 and the neighboring carbonyl oxygen of the Suc ring, $N^1H•O^1C$. **[Suc+H]$^+$-1.4** (Figure S2), which lies only ~0.3 kJ/mol higher than **1.3**, has the same hydrogen bond and differs only in the ∠CN^2CC dihedral angle. **[Suc+H]$^+$-4.1**, the B3LYP and B3P86 GS at both 0 and 298 K, forms a hydrogen bond between the protonated O^{s1} carbonyl and the Ser hydroxyl oxygen, $O^{s1}H•O^{s2}H$, whereas **4.2**, merely rotates the amino group (as does **4.4**, Figure S2). In contrast, **4.3**, forms a hydrogen bond with the carboxylic acid carbonyl oxygen, $O^{s1}H•O^2C$. In **[Suc+H]$^+$-2.1**, the protonated ring carbonyl hydrogen bonds to the carbonyl oxygen of the carboxylic acid group, $O^1H•O^2C$, and the amino group orients to interact with O^1 as well. The related structure **2.2** simply rotates the amino group while maintaining the $N^1H•O^2$ hydrogen bond. In **2.3**, rotation of the $NCCO^{s2}$ dihedral repositions the hydroxyl group while maintaining the key hydrogen bonds. **2.4** and **2.5** (Figure S2) have similar energies as **2.3** and simply rotate the amino group and/or hydroxyl hydrogen.

The lowest energy $[Fur+H]^+$ structures protonate at N^2 (site 3 in Scheme 1) and are characterized by $N^2H•N^1$ hydrogen bonds, such that the $[Fur+H]^+$-3 isomers are distinguished primarily by the orientation of the Ser side chain. As shown in Figure 3d, the Ser side chain in **[Fur+H]$^+$-3.1** is directly involved with the protonation site, yielding a $N^2H•O^{s2}H$ hydrogen bond. In **[Fur+H]$^+$-3.2** and **3.3**, there is an $N^2H•O^2C$ hydrogen bond instead. In **3.2**, the side chain interacts with the hydroxyl oxygen of the carboxylic acid, $O^{s2}H•O^3$, whereas this interaction is eliminated in **[Fur+H]$^+$-3.3**. The $N^2H•O^{s2}H$ hydrogen bond is strongly preferred, as **[Fur+H]$^+$-3.2** and **3.3** are located 18 – 26 kJ/mol higher in energy than the **[Fur+H]$^+$-3.1** GS, Table 2.

Theoretical Results for Deamidation of [AsnSer+H]$^+$. Pathways yielding succinimide and furanone structures via deamidation of $[AsnSer+H]^+$ parallel those found previously for the analogous dissociation of $[AsnThr+H]^+$.[20] For furanone formation, proton transfer to the side-chain amide nitrogen from the protonated N^1-terminus results in the formation of the NH_3 leaving group and C–NH_3 bond elongation. Further elongation results in concomitant motions of bond rupture and furanone ring formation via $TS_{N\text{-}Fur}$, Figure 4, 134 – 145 kJ/mol above the $[AsnSer+H]^+$-1 GS.

Loss of NH_3 leads to **[Fur+H]$^+$-3.1** + NH_3 (129 – 144 kJ/mol above the GS, 5 – 9 kJ/mol below $TS_{N\text{-}Fur}$ at the B3LYP and B3P86 levels and 10 kJ/mol higher than $TS_{N\text{-}Fur}$ at the MP2 level). Although MP2 suggests a product limited pathway, because the tight $TS_{N\text{-}Fur}$ is close in energy to the product asymptote, $TS_{N\text{-}Fur}$ may still play a major role in controlling the rate of the reaction.

A competitive pathway leading to succinimide formation was also located. Here, proton transfer from the peptide bond nitrogen (N^2) to the Asn side-chain amide nitrogen yields the NH_3 leaving group. C–NH_3 bond elongation results in bond rupture and succinimide ring formation via $TS_{N\text{-}Suc}$ (Figure 4, 130 – 151 kJ/mol above the GS), which is the rate-limiting step in this reaction. The NH_3 remains hydrogen bound to the side-chain hydroxyl oxygen in the following intermediate. Note that in this TS, O^1 (site 2 in Scheme 1) of the incipient Suc product is protonated, such that simple loss of ammonia would form **[Suc+H]$^+$-2.y**. **[Suc+H]$^+$-1.y** can be formed by proton transfer from O^1 to N^1 (site 1), which should be facile given the proximity of these two sites (Figure 3). This proton transfer may also be facilitated by the ammonia group before it is expelled. We also looked for a pathway to form **[Suc+H]$^+$-4.y**. A precursor intermediate similar to that leading to $TS_{N\text{-}Suc}$ was located, but now proton transfer from the peptide bond nitrogen to the side-chain amide is inhibited such that no TS leading to proton transfer and ring closure was found. It is possible that generation of **[Suc+H]$^+$-4.y** could be facilitated by proton transfer from **2.y** involving the NH_3 group before its expulsion, but cursory attempts to locate such a pathway were not successful.

Overall, the rate-limiting step for furanone formation is lower in energy than that for succinimide formation by 13 kJ/mol at the B3LYP level, but higher in energy at the B3P86 and MP2 levels by 3 and 14 kJ/mol, respectively. These energetic results explain why spectral signatures indicative of both furanone and succinimide deamidation products are observed in the IRMPD studies, as detailed in the next section. Because these products are also distinguished by different decomposition pathways, we also evaluated mechanisms leading to NH_3 and H_2O loss from the $[Fur+H]^+$ and $[Suc+H]^+$ structures (see Figures S3 – S5). The lowest energy pathway for secondary ammonia loss (yielding *m/z* 186) was located for $[Fur+H]^+$, with rate-limiting energies

of 312 – 327 kJ/mol relative to the $[AsnSer+H]^+$ GS (Figure S3), 183 – 186 kJ/mol above **$[Fur+H]^+$-3.1**. Although we looked for a pathway for dehydration of **$[Fur+H]^+$-3.y**, no competitive mechanism was located. In contrast, secondary dehydration of $[Suc+H]^+$ (forming *m/z* 185) is energetically reasonable, yielding a bicyclic species (Figure S4). The dehydration TS is rate-limiting for B3LYP and B3P86 (239 – 250 kJ/mol above the GS), whereas the products are rate-limiting for MP2 (225 kJ/mol above the GS). These rate-limiting steps lie 112 – 134 kJ/mol above the primary product. This dehydration channel is at least 100 kJ/mol lower in energy than the alternative sequential ammonia loss from $[Suc+H]^+$ (Figure S5). Thus, these theoretical results suggest that $[Fur+H]^+$ should decompose by loss of ammonia, whereas $[Suc+H]^+$ is more likely to fragment by dehydration.

Spectroscopic Determination of the Deamidation Product Ion, $[AsnSer+H-NH_3]^+$. Experimentally, the deamidation product of protonated AsnSer ($[AsnSer+H-NH_3]^+$, *m/z* 203) was produced by CID with He and isolated in the quadrupole ion trap. IRMPD of this product ion yielded major fragments observed at *m/z* 186 ($–NH_3$), 185 ($–H_2O$), 161 ($–CH_2CO$), 157 ($–CO–H_2O$), 143 ($–H_2O–CH_2CO$), 140 ($–NH_3–CO–H_2O$), 129 ($–2CO–H_2O$), 116 ($C_4H_6O_3N^+$), 88 ($C_3H_6O_2N^+$), and 71 ($C_3H_3O_2^+$), as shown in Figure S6 of the Supporting Information. This figure also shows that irradiation at different wavelengths produces different fragmentation patterns. Among the major fragments, it was found that fragmentation into *m/z* 186 and 161 channels shows similar wavelength dependence, whereas the spectral responses for *m/z* 185, 157, and 88 channels are similar to each other and significantly different from those of *m/z* 186 and 161.

The two IRMPD spectra obtained from fragments *m/z* 186+161 and from *m/z* 185+157+88 are shown in Figure 5, where it can be seen that they both share bands at 986 and 1954 cm^{-1}, but these bands are quite weak in the *m/z* 185 + 157 + 88 spectrum. Indeed, as shown in Figure 5, if the *m/z* 186 + 161 spectrum is scaled down, it reproduces both of these bands in the *m/z* 185 + 157 + 88 spectrum with the correct relative intensity. Furthermore, although not shown in Figure 5, two bands at 726 and 763 cm^{-1} are also found in both spectra with the correct relative intensities. Such observations suggest the presence of two different isomers of $[AsnSer+H-NH_3]^+$, with the

m/z 186 + 161 spectrum representing one species and the *m/z* 185 + 157 + 88 representing the other, along with a small amount of the first isomer.

Figure 5 compares the two individual experimental spectra for $[AsnSer+H-NH_3]^+$ and several calculated spectra for both **[Fur+H]**$^+$ and **[Suc+H]**$^+$ species. Comparison between the experimental spectrum and additional higher-lying species is given in the Supporting Information, Figure S7. The two experimental spectra differ in several respects, but most notably by the intense band at 1954 cm^{-1} in the spectrum observed via channels *m/z* 186 and 161. This band is reproduced well by **[Fur+H]**$^+$**-3.1**, which has a predicted band at 1959 cm^{-1} (ring C=O stretch). This assignment is also consistent with the theoretical evaluation above, which indicated that $[Fur+H]^+$ can dissociate by loss of NH_3 (forming *m/z* 186). Further, this conformer predicts bands at 1784 (C=O stretch and COH bend of terminal carboxylic acid) and 1688 (C=N stretching of the imine bond) cm^{-1}, which agree nicely with experimental bands at 1784 and 1702 cm^{-1}. Lower-intensity bands at 1627, 1482, 1154, 986, and 947 cm^{-1} in the experimental spectrum are also predicted fairly well by **[Fur+H]**$^+$**-3.1** via calculated bands at 1630 (NH_2 bending of the amine moiety), 1479 (HNC bend of the imine bond), 1167 (primarily COH bend of Ser side chain and NH wag) and 1149 (COH bend of terminal carboxylic acid), 961 and 921 cm^{-1} (delocalized motions of the furanone ring). Also shown in Figure 5 is a comparison to **[Fur+H]**$^+$**-3.2**. As discussed above, differences in the **3.y** conformers are the result of changes in the orientation of the C-terminus such that the predicted spectral response is similar for these species, with minor deviations in the low-frequency region. **[Fur+H]**$^+$**-3.2** predicts bands similar to those of **[Fur+H]**$^+$**-3.1**: 1967, 1773, 1687, 1630, 1478, 1158, 955, and 914 cm^{-1}. Although not shown, **[Fur+H]**$^+$**-3.3** is very similar to **3.2** with predicted bands at 1964, 1763, 1693, 1631, 1471, 1160, 955, and 916 cm^{-1}. Therefore, on a spectral basis, contributions from these isomers cannot be ruled out; however, according to the B3LYP, B3P86, and MP2 Gibbs energies, Table 2, an equilibrium distribution of $[Fur+H]^+$ conformers at 298 K would have a >99% population of **[Fur+H]**$^+$**-3.1**. Thus, we identify **[Fur+H]**$^+$**-3.1** as the conformer formed experimentally.

As shown in Figure 5, the spectrum constructed from fragments *m/z* 185 + 157 + 88 differs from that of *m/z* 186 + 161. The experimental *m/z* 185 + 157 + 88 spectrum has prominent features centered at 1749, 1605, 1487, 1402, 1341, 1149, and 1078 cm^{-1}. As noted above, weak bands at 986 and 1953 cm^{-1} appear to be a small contribution from **[Fur+H]$^+$-3.1** in these mass channels. Arguably, **[Suc+H]$^+$-1.1** exhibits a reasonable reproduction of this experimental spectrum. **[Suc+H]$^+$-1.1** has predicted major bands at 1758 (anti-symmetric C=O stretches of succinimide ring); 1694 (C=O stretch and COH bend of terminal carboxylic acid); 1637 and 1599 (NH motions of the amine protonation site); 1507 (NH_3 umbrella); 1403 (carboxylic acid COH bend and side-chain CH_2 wag); 1363 and 1331 (primarily CH bends and side-chain COH bend); 1312 (delocalized ring CN stretches and NCH bends); 1172 and 1164 (primarily COH bends of carboxylic acid and Ser side chain); and 1070 (primarily CO stretch of Ser side chain) and 1048 (side-chain COH bend and CC ring stretch) cm^{-1}. **[Suc+H]$^+$-1.2** has a similar spectrum (Figure S7) and hence is not shown here. Likewise, **[Suc+H]$^+$-1.3** and **1.4** have similar spectra that differ from **1.1** and **1.2** because the carboxylic acid carbonyl is no longer hydrogen bonded to the protonation site. **[Suc+H]$^+$-1.3** is predicted to show bands at 1835 (symmetric C=O stretches of succinimide ring); 1771 (C=O stretch and COH bend of terminal carboxylic acid); 1748 (anti-symmetric C=O stretches of succinimide ring); 1624 and 1601 (NH motions of the amine protonation site); 1460 (NH_3 umbrella); 1393, 1376, and 1364 (primarily CH motions of the succinimide ring and peptide backbone); 1332 (COH bend of the carboxylic acid along with CH wag); 1143 (COH bends of carboxylic acid and Ser side chain); and 1040 (primarily CO stretch of Ser side chain) cm^{-1}. Clearly, the hydrogen bonding differences in these pairs of structures lead to distinct positions of the carbonyl stretches, the NH_3 umbrella vibration, as well as other modes. Given these spectral comparisons, the possibility that any of these low-energy **[Suc+H]$^+$-1.y** structures contributes to the spectrum cannot be eliminated.

Figure 5 also includes a comparison to **[Suc+H]$^+$-4.1**, the B3LYP and B3P86 GS at 0 and 298 K. The **4.1** and **4.2** isomers have very similar spectra (Figure S7). Here, major bands are found at 1843 (ring C=O^1 stretch); 1786 (carboxylic acid C=O stretch); 1593 (ring C=O^{s1} stretch); 1555

(ring $CO^{s1}H$ bend); 1392 (ring $CO^{s1}H$ bend coupled with CH bends); 1151 (carboxylic COH bend); 1059 (side-chain C-OH stretch and ring stretches); and 968 ($O^{s1}H$ wag) cm^{-1}. Clearly, **4.y** species alone do not reproduce the broad experimental band at 1749 cm^{-1}, and the predicted intensity of the bands at 1843 and 1593 cm^{-1} are much larger than experiment. Therefore, the **[Suc+H]$^+$-4.y** species cannot be the dominant product formed, but could contribute to the observed spectrum, helping to explain the width of the high-frequency band peaking at 1749 cm^{-1}, matching the peak observed at 1605 cm^{-1}, and adding to the peaks observed at 1402, 1149, and 1078 cm^{-1}.

As noted above, we did not locate a reasonable pathway that would generate the **[Suc+H]$^+$-4.y** species. Therefore, we also considered the [**Suc+H]$^+$-2.y** species, which do lie along the pathway for **[Suc+H]$^+$-1.y** formation. For the **2.1** conformer shown in Figure 5, there are major bands at 1845 (ring CO^{s1} stretch); 1724 (carboxylic acid CO stretch, redshifted by the $O^1H\bullet O^2C$ hydrogen bond); 1592 (ring CO^1 stretch); 1505 (ring CO^1H bend); 1423 (Ser CH bends); 1166 and 1186 (symmetric and asymmetric Ser side-chain and carboxylic COH bends); 1074 and 1081 (Ser CH bends and ring stretches); and 987 (O^1H wag) cm^{-1}. **[Suc+H]$^+$-2.2** exhibits a similar spectrum with similarly identified bands at 1849, 1723, 1600, 1518, 1426, 1165 and 1183, 1057, and 989 cm^{-1}. Bands near 1100 cm^{-1} differ between the two isomers, with **2.2** having bands at 1098 (ring stretches) and 1061 (CO^{s2} stretch) cm^{-1}. As for the **4.y** species, the **2.y** species cannot be the dominant product formed, but the intense 1724 cm^{-1} band of **2.1** falls between the intense 1758 and 1694 bands of **1.1**, such that a combination of the two matches the width of the experimental 1749 cm^{-1} band. Further, **2.1** reproduces the peaks observed at 1605 cm^{-1} (with a better intensity than **4.1**), 1402, and 1078 cm^{-1}, while also contributing to the peaks observed at 1487 and 1149 cm^{-1}.

Importantly, none of the low-energy $[Suc+H]^+$ species located predict a band at 1953 cm^{-1}, consistent with our assignment of this low-intensity feature as a minor contribution to the *m/z* 185, 157, and 88 product ions coming from the furanone structure. This can be seen in Figure S6 for irradiation at 1961 cm^{-1}. We conclude that a combination of **[Suc+H]$^+$-1.1** and **2.1** structures is likely responsible for the *m/z* 185 + 157 + 88 spectrum, although contributions of other **1.y**, **2.2**,

and possibly **4.y** structures are also feasible. Notably, the generation of $[Fur+H]^+$ species clearly shows that the $[AsnSer+H-NH_3]^+$ species are not formed under equilibrium conditions, such that the distribution of isomers is controlled by kinetic effects. Importantly, the assignment of this spectrum to the succinimide is consistent with the calculations indicating that dehydration from $[Suc+H]^+$ (forming *m/z* 185) is a lower energy process than loss of ammonia and that the furanone structure does not readily dehydrate.

Population Analysis of Deamidation Products. The IRMPD spectra for $[AsnSer+H-NH_3]^+$ described above suggest that there are two distinct product ion structures in the *m/z* 203 population. Figure 6 shows the result of a population analysis that allows an estimate of the approximate relative abundance of the two structures.[45-48] To achieve this, the IR laser was tuned to a frequency where one of the isomers absorbs but the other is transparent. As the irradiation was performed with an increasing number of IR pulses, complete dissociation of the absorbing isomer can be achieved while leaving the other isomer intact.

At a frequency of 1961 cm^{-1}, only the furanone isomer absorbs while the succinimide has no absorption in this range of the spectrum (see Figure 5). Prolonged irradiation at this frequency is therefore assumed to induce complete depletion of the furanone ion population, while leaving the succinimide isomer unaffected. Figure 6 shows that with an increasing irradiation length, the *m/z* 203 ion population decreases and finally levels off to a constant value, which is not zero. The remaining fraction, which is 70 ± 2% of the original *m/z* 203 peak intensity, is attributed to the succinimide ion population. This result suggests that formation of the succinimide is more favorable than the furanone, a conclusion consistent with the relative energies of $TS_{N\text{-}Fur}$ and $TS_{N\text{-}Suc}$ at the B3P86 and MP2 levels (Figure 4).

Unfortunately, there is no band that is unique to the succinimide isomer. Therefore, additional traces in Figure 6 show analogous analyses, but with the laser tuned to 1780 and 967 cm^{-1}. At 1780 cm^{-1}, both isomers have strong absorption bands. Prolonged irradiation indeed leads to rapid depletion of the *m/z* 203 ion population. At 967 cm^{-1}, the furanone isomer has a significant absorption band, whereas the succinimide shows weak absorption. This curve reflects these

disparate absorptions as a slowly decaying *m/z* 203 population, slowly reaching near-complete depletion.

Structures of the Dehydration Product Ion, [AsnSer+H-H_2O]$^+$. Dehydration of many dipeptides, via b/y-type fragmentations, involves loss of the C-terminal hydroxyl group, leading to an oxazolone structure.[49-53] As noted in the introduction, in a recent paper,[22] the dehydration product ions formed from several protonated XxxSer and XxxThr (including Xxx = Asn) dipeptides were examined using IR action spectroscopy coupled with quantum-chemical calculations. This work showed that dehydration produces oxazoline structures [OxaI+H]$^+$, rather than the oxazolone [OxaO+H]$^+$ expected for dehydration at the C-terminus. A second structure was also indicated for AsnSer and tentatively suggested to be the thermodynamically favored monoketopiperazine [MKP+H]$^+$ product, which is formed by H_2O expulsion from the Ser side chain via attack by the N-terminal amino nitrogen. In the present work, our calculations revealed several additional structures for various possible dehydration products, such that we reexamine the dehydration process of [AsnSer+H]$^+$ more thoroughly here.

Previously, five possible structures for [AsnSer+H-H_2O]$^+$ were considered: 1) diketopiperazine (DKP), 2) OxaO, 3) MKP, 4) OxaI, and 5) pyrrolidone (Pyr). These structures are illustrated in Scheme 3 along with the lowest energy protonation sites found. (In the previous work, all possible protonation sites were examined and only the lowest of these is included here.) The clear ground structure at all levels of theory was **[MKP+H]$^+$-3.4.1** (protonation at site 4, one of the ring nitrogens). Low energy structures for the various isomers are summarized in Table 3 and include **[DKP+H]$^+$-1.3** and **1.5**, **[OxaO+H]$^+$-2.4**, **[OxaI+H]$^+$-4.1** and **4.4**, and **[Pyr+H]$^+$-5.3**. These structures have relative energies that are 19 – 52 kJ/mol lower in energy than previously identified,[22] except for the oxazoline species where the energies are about 5 kJ/mol lower than previously reported.

Theoretical Results for Dehydration of [AsnSer+H]$^+$. In our previous study,[22] three pathways for dehydration of a model system, [GlySer+H]$^+$, were examined in detail. 1) The simplest of these was a direct transfer of a proton from the protonated amide oxygen to the serine

hydroxyl group followed by ring closure. Despite its straightforward nature, this pathway was found to have the highest barrier, 231 kJ/mol above the ground structure (GS) for $[GlySer+H]^+$ at the MP2/6-311+G(2d,2p)//B3LYP/6-31++G(d,p) level. 2) A pathway originally proposed by Reid and O'Hair for dehydration of Acetyl-Ser-OH [54] involves proton transfer to the serine hydroxyl group and backside nucleophilic attack by the amide oxygen, leading to the oxazoline product. In the $[GlySer+H]^+$ system, this TS lies 140 kJ/mol above the GS; however, the intermediate needed to reach this TS involves a geminal diol complex at the C-terminus and formation of this species passes over a barrier of 158 kJ/mol above the GS. 3) A pathway originally elucidated in our previous study of $[AsnThr+H]^+$ involves a tetrahedral intermediate in which the oxazoline ring has already been formed.[20] Briefly, the mobile proton must transfer to the amide oxygen, such that nucleophilic attack by the Thr (or Ser) hydroxyl oxygen at the electrophilic amide carbon leads to ring formation and the tetrahedral intermediate. In the $[AsnThr+H]^+$ system, the Asn side-chain oxygen acts as the proton accepting nucleophile,[20] whereas in $[GlySer+H]^+$ (or any peptides not containing a nucleophilic side chain in the first residue), the N-terminal nitrogen acts as the proton accepting nucleophile.[22] In the $[GlySer+H]^+$ system, this TS was the rate-limiting step, 97 kJ/mol above the GS; whereas the availability of the Asn side-chain reduces the energy of the analogous TS. Once the tetrahedral intermediate is formed, it rearranges such that the protonated N-terminus moves to a position where it can transfer the proton to the hydroxyl group (the protonated carbonyl of the dipeptide linkage) leading to water expulsion (notably containing the backbone amide oxygen, H_2O^1). In the $[GlySer+H]^+$ system, two similar TSs were identified, lying 77 and 112 kJ/mol above the GS. These two TSs are distinguished by whether the carboxylic acid group lies on the same side of the five-membered ring (where it can assist in stabilizing the water formation) or on the other side, respectively. In any event, it is clear that the mechanism for dehydration involving the tetrahedral intermediate is the lowest energy pathway among the three proposals. Because there are nuances to this pathway not completely captured in the previous work on $[GlySer+H]^+$, this mechanism was explored thoroughly in the present system.

For $[AsnSer+H]^+$, formation of the $[OxaI+H]^+$ product passes through tetrahedral intermediates, of which two distinct conformers were located. These tetrahedral intermediates can be formed from the GS reactants via proton transfer from the serine hydroxyl side chain to either the carboxamide side chain or to the N terminus. From the two tetrahedral intermediates, we located seven distinct dehydration TSs leading to oxazoline formation. The lowest energy pathways proceeding through each intermediate are shown in Figure 7 and Supporting Information Figure S8 includes all the pathways described below.

The two tetrahedral intermediates, $INT_{O\text{-}OxaI\text{-}c}$ and $INT_{O\text{-}OxaI\text{-}t}$ (Figure 7, where the subscript O indicates dehydration and OxaI refers to the eventual oxazoline product), are distinguished by the stereochemistry at the tetrahedral site, which positions the carboxylic acid group either cis (c) or trans (t) relative to the hydroxyl group attached to the tetrahedral center. The energies of these two species are very similar, 30 – 49 and 32 – 52 kJ/mol, respectively, relative to the $[AsnSer+H]^+$-1 GS.

For generation of the tetrahedral intermediates, the molecule first must protonate the carbonyl oxygen of the first residue. Then proton transfer from the serine hydroxyl side chain to the carboxamide side chain yields $TS_{O\text{-}OxaI\text{-}tet\text{-}Oc}$ (Figure S8) and $TS_{O\text{-}OxaI\text{-}tet\text{-}Ot}$ (Figure 7), which then form the cis and trans tetrahedral intermediate, respectively. For the trans isomer, this TS is the lowest-energy pathway, whereas for the cis isomer, there is a lower-energy pathway (by 10 – 15 kJ/mol) found that involves proton migration to the N-terminus, $TS_{O\text{-}OxaI\text{-}tet\text{-}Nc1}$ (Figure 7). Additional TSs leading to each intermediate that utilize proton transfer to the N-terminus were also located: $TS_{O\text{-}OxaI\text{-}tet\text{-}Nc2}$, $TS_{O\text{-}OxaI\text{-}tet\text{-}Nt1}$, and $TS_{O\text{-}OxaI\text{-}tet\text{-}Nt2}$, which lie above the lower energy TSs by 31 – 39, 22 – 27, and 40 – 46 kJ/mol, respectively. Note that utilizing the N-terminus is a pathway available for all amino acid residues and the only one available for a species like $[GlySer+H]^+$. In that case, this TS is the rate-limiting step in the overall dehydration process.

From each of these tetrahedral intermediates, multiple TSs for dehydration can be found and involve protonation of the O^1H hydroxyl group on the tetrahedral center, leading to water formation. If the protonated N-terminus supplies the proton, there are four TSs located, two from

each tetrahedral intermediate. These differ only in the relative orientations of the two residues, as indicated by the NCCN dihedral angle, either gauche (g) or trans (t). Of these, the one having the lowest energy is $TS_{O\text{-}OxaI\text{-}Ngc}$ (Figure S8), with the ∠NCCN dihedral angle being g and the carboxylic acid group being cis (c) to the water. Close in energy is $TS_{O\text{-}OxaI\text{-}Ntc}$, which differs only in the orientation of the NCCN dihedral angle. In contrast, $TS_{O\text{-}OxaI\text{-}Ntt}$ and $TS_{O\text{-}OxaI\text{-}Ngt}$ lie 10 – 20 kJ/mol higher in energy because the carboxylic acid no longer helps stabilize the water formation. Alternatively, the asparagine side chain can supply the proton yielding water formation. From $Int_{O\text{-}OxaI\text{-}t}$, we located both $TS_{O\text{-}OxaI\text{-}Ogt1}$ (Figure S8) and $TS_{O\text{-}OxaI\text{-}Ogt2}$ (Figure 7), which have similar energies as $TS_{O\text{-}OxaI\text{-}Ntt}$. For the pathway proceeding through $INT_{O\text{-}OxaI\text{-}t}$, any of these dehydration TSs could be the rate-limiting step, 121 – 137 kJ/mol above the GS. For the pathway proceeding through $INT_{O\text{-}OxaI\text{-}c}$, we located one TS where the Asn side chain facilitates protonation of the hydroxyl group, $TS_{O\text{-}OxaI\text{-}Ogc}$ (Figure 7), which lies considerably lower than the other dehydration TSs, 75 – 93 kJ/mol above the GS. Thus, this pathway is limited by formation of the cis tetrahedral intermediate at $TS_{O\text{-}OxaI\text{-}tet\text{-}Nc1}$, 92 – 113 kJ/mol above the GS (Figure 7). This is the lowest-energy pathway, although a weighted average of the various pathways might actually be sampled experimentally.

In our previous work on the $[AsnThr+H]^+$ system, the pathway located for formation of the oxazoline dehydration product was the equivalent of $TS_{O\text{-}OxaI\text{-}tet\text{-}Ot}$ forming $INT_{O\text{-}OxaI\text{-}t}$, which dehydrates via either $TS_{O\text{-}OxaI\text{-}Ntt}$ or $TS_{O\text{-}OxaI\text{-}Ogt1}$, and the lower energy pathway through $INT_{O\text{-}OxaI\text{-}c}$ was not considered. In that work, the experimental threshold energy for dehydration was measured as 117 ± 5 kJ/mol, in reasonable agreement with the theoretical energies of $TS_{O\text{-}OxaI\text{-}Ntt}$, 116 – 130 kJ/mol at the same levels of theory used here. As found here for the analogous $[AsnSer+H]^+$ system, $TS_{O\text{-}OxaI\text{-}Ogt1}$ had a very similar energy. In that study, very similar energies were obtained for dehydration to produce an oxazolone product (by elimination of the carboxylic acid hydroxyl group), with a rate-limiting $TS_{O\text{-}OxaO}$ at 120 – 129 kJ/mol above the GS. If we now calculate the pathway for dehydration via the cis tetrahedral intermediate, we find that $TS_{O\text{-}OxaI\text{-}tet\text{-}Oc}$ is unavailable because the added methyl group limits access to the carbonyl of the side chain.

Hence, formation of the intermediate is limited by $TS_{O\text{-}OxaI\text{-}tet\text{-}Nc1}$, lying 89 – 111 kJ/mol above the GS. $TS_{O\text{-}OxaI\text{-}Ngc/Ntc}$ for dehydration of the $[AsnThr+H]^+$ cis tetrahedral intermediate lies 96 – 119 kJ/mol above the GS, and $TS_{O\text{-}OxaI\text{-}Ogc}$ lies 66 – 84 kJ/mol above the GS. Thus, this pathway is limited by $TS_{O\text{-}OxaI\text{-}tet\text{-}Nc1}$, which is slightly lower than the experimental threshold, but well below the pathway for oxazolone formation. Experimentally, IRMPD results showed exclusive formation of the oxazoline, more consistent with this revised computational result.

Similarly, in the present $[AsnSer+H]^+$ system, formation of the oxazolone product, $[OxaO+H]^+$, passes over the rate-limiting $TS_{O\text{-}OxaO}$ (Supporting Information Figure S9) lying 120 – 130 kJ/mol above the GS, with the oxazolone + H_2O products lying 11 – 27 kJ/mol lower than $TS_{O\text{-}OxaO}$. The lowest energy pathway yielding the $[OxaI+H]^+$ product described above is lower in energy by 16 – 38 kJ/mol. The resulting $[OxaI+H]^+$ + H_2O products are located 28 – 54 kJ/mol below $TS_{O\text{-}OxaI\text{-}tet\text{-}Nc1}$ and 40 – 44 kJ/mol lower in energy than the alternative oxazolone structure. The comparison of the rate-limiting TSs for oxazolone and oxazoline formation are consistent with not observing the former product in the IRMPD results (see below).

As noted above, previous IRMPD results indicate that $[OxaI+H]^+$ is not formed exclusively in the dehydration of $[AsnSer+H]^+$.[22] The authors proposed several different possible isomers but explicit pathways leading to each of these products were not fully explored. Therefore, we tried looking for pathways to generate these products, although an exhaustive search was not conducted. The lowest pathway for formation of $[MKP+H]^+$ has a rate-limiting step located 202 – 214 kJ/mol above the GS, meaning that this pathway should not be competitive with the $[OxaI+H]^+$ processes described above. Likewise, we could not locate a pathway in which $[Pyr+H]^+$ formation involved a low-energy TS (the rate-limiting step, which involves formation of a tetrahedral intermediate and the five-member pyrrolidone ring, was calculated to lie 212 – 266 kJ/mol above the GS). However, a competitive pathway was located for $[DKP+H]^+$ formation with a rate-limiting step lying 108 – 121 kJ/mol above the $[AsnSer+H]^+$ GS. An overview of key TS and intermediate structures found here is given in Figure S10. Notably, formation of DKP requires a cis/trans isomerization of the peptide bond, but the TS for this transformation lies only 71 – 77 kJ/mol above

the GS reactants. The rate-limiting step involves formation of a tetrahedral intermediate and the six-member DKP ring. Overall, the rate-limiting step for $[DKP+H]^+$ formation lies 7 – 16 kJ/mol above the lowest energy pathway for $[OxaI+H]^+$, suggesting that these two species could compete.

Spectroscopic Structure Determination of the Dehydration Product Ion, [AsnSer+H-H_2O]$^+$. The $[AsnSer+H-H_2O]^+$ product (*m/z* 202) was observed to photodissociate via three main channels: loss of ammonia to yield *m/z* 185, formation of *m/z* 87 ($[IPA+H]^+$, Scheme 2), and formation of *m/z* 143 (loss of $NH_2C(=O)CH_3$ from $[AsnSer+H-H_2O]^+$ or loss of ketene from *m/z* 185), each of which exhibited different appearance spectra. Loss of ammonia exhibited a spectrum comparable to that found for the sum of all products (shown in ref. 22), which has three distinct bands in the carbonyl stretch region near 1700, 1750, and 1800 cm^{-1}. In contrast, the IR spectrum imprinted into channel *m/z* 87 has bands near 1700 and 1800 cm^{-1} but not near 1750 cm^{-1}. As shown in ref. 22, this spectrum is reproduced with excellent fidelity by the oxazoline structure $[OxaI+H]^+$-**4.1**, with predicted bands at 1689 cm^{-1} (C=O stretch of carboxamide group) and 1802 cm^{-1} (C=O stretch of carboxylic acid group). This structure also reproduces an intense band observed at 1136 cm^{-1}, corresponding to the COH bend of the carboxylic acid group predicted at 1142 cm^{-1}. (Also the oxazoline structure shown in ref. 22 is **4.1.2**, which is not the lowest energy structure at the levels of theory explored here. Rotation of the carboxylic acid group by about 180° leads to **4.1.1**, lower by 0.0 – 1.4 kJ/mol, Table 3. Nevertheless, **4.1.1** and **4.1.2** have very similar spectra.) This assignment is also consistent with the fact that only the oxazoline and oxazolone structures have a side-chain group corresponding to the *m/z* 87 product (Scheme 3), but the oxazolone structures do not have predicted bands at 1800 and 1140 cm^{-1}.

Figure 8 shows the IRMPD spectrum observed in the *m/z* 143 fragment channel. It retains the three high-frequency bands near 1700, 1750, and 1800 cm^{-1} but compared to the spectrum for all products, the intensity of the 1750 band is larger while the relative intensities of the 1700 and 1800 cm^{-1} bands remain similar. The $[OxaI+H]^+$-**4.1.1** again reproduces much of this spectrum but fails to include intensity at 1750 cm^{-1}, as well as at 1457 and 1038 cm^{-1}. Candidates for reproducing the 1750 cm^{-1} band include $[MKP+H]^+$-**3.4.1**, the lowest energy product located, and $[DKP+H]^+$-

1.5.1. In both cases, this band corresponds to the C=O stretch of the piperazine ring (predicted at 1747 and 1752 cm^{-1}, respectively). In ref. 22, the $[MKP+H]^+$-**3.4.1** species was tentatively assigned largely because of its low energy and because it reproduces the broad experimental band peaking near 1450 cm^{-1} and has intensity in the 1200 – 1350 cm^{-1} range. The same can also be said of the $[DKP+H]^+$-**1.5.1** species, which now has a relative energy comparable to the $[OxaI+H]^+$-**4.1.1** species (lower at most levels of theory, Table 3). One could argue that the two bands of the $[MKP+H]^+$-**3.4.1** structure at 1107 and 1160 cm^{-1} are not particularly consistent with the sharp band observed at 1136 cm^{-1} (assigned to $[OxaI+H]^+$-**4.1.1**), whereas no such bands are present for the DKP species. It may also be interesting to note that the spectrum for all products shows one additional high-frequency (but very low intensity) band near 1850 cm^{-1}, which could possibly be explained by the $[Pyr+H]^+$-**5.3.1** product (C=O stretch of pyrrolidone ring), although its population cannot be very high. Overall, the spectroscopic evidence clearly indicates that the dominant species formed is $[OxaI+H]^+$-**4.1.1** and that either $[MKP+H]^+$ or $[DKP+H]^+$ is also formed. The theoretical results discussed above include a competitive pathway for $[DKP+H]^+$ formation (but not $[MKP+H]^+$), suggesting that the diketopiperazine product is probably the species formed along with $[OxaI+H]^+$-**4.1.1**.

Cross Section Modeling. Using eq 1, thresholds for the primary competitive deamidation and dehydration channels from the decomposition of $[AsnSer+H]^+$ were analyzed. Both primary channels were modeled simultaneously in order to account directly for competition. Here, the cross section for the dehydration reaction was correlated with the sum of *m/z* 202 and its sequential *m/z* 87 product and that for the deamidation reaction with the sum of *m/z* 203 and its sequential deamidation product *m/z* 186. The zero-pressure extrapolated deamidation and dehydration data were fully reproduced using parameters given in Table 4, as shown in Figure 9. TS frequencies used for the cross section modeling were taken from the theoretical results discussed above. As will be seen, low-frequency modes of some TSs are modified slightly in order to be able to reproduce the relative shapes (energy dependences) and magnitudes of the competing product cross sections. As pointed out in the work where we originally used this approach [55], similar results

can be obtained by scaling the magnitudes of the cross section models, but scaling factors approaching $10^3 - 10^6$ were needed, which is physically unmeaningful. In contrast, as pointed out in the Gaussian 16 program, calculations of vibrational frequencies below about 900 cm^{-1} are subject to considerable uncertainty because they may no longer be accurately treated as harmonic, and it is only these frequencies that are adjusted. We first analyzed the data using the tight $TS_{N\text{-}Fur}$ (Figure 4) and $TS_{O\text{-}OxaI\text{-}tet\text{-}Nc1}$ (Figure 7) parameters for deamidation and dehydration, respectively. (Although the MP2 level of theory predicts a product limited pathway for deamidation, $TS_{N\text{-}Fur}$ lies only 10 kJ/mol below the product asymptote at this level. Thus, this TS can still limit product formation at energies only slightly above the product asymptote. Therefore, these data were fit using parameters for $TS_{N\text{-}Fur}$, consistent with the B3LYP and B3P86 prediction of a tight TS limited pathway.) Our analysis shows that in order to fit the data accurately in the threshold region as well as over the full energy range, the low-frequency modes (<900 cm^{-1}) for $TS_{O\text{-}OxaI\text{-}tet\text{-}Nc1}$ needed to be tightened by ~7% while holding those for the major $TS_{N\text{-}Fur}$ channel constant. Such scaling results in a good reproduction of the data throughout the threshold region, Figure 9. Given the possibility to also form $[Suc+H]^+$ (on the basis of the theoretical energy competition between succinimide and furanone formation as well as the IRMPD data), the data were also modeled using molecular parameters for succinimide formation. Here, a comparable fit (to that obtained via $TS_{N\text{-}Fur}$ modeling) was achieved using parameters also given in Table 4, where this approach required more frequency scaling ($TS_{O\text{-}OxaI\text{-}tet\text{-}Nc1}$ tightened by about 17%) in order to fit the data in the threshold region. This approach yields a similar (although slightly lower) threshold for dehydration, whereas the threshold for deamidation decreases by ~15 kJ/mol. The change in the deamidation threshold energy for the Fur versus Suc pathways occurs because the latter pathway is entropically less favorable, as indicated by the very distinct activation entropies, $\Delta S^{\dagger}_{1000}$ in Table 4. For furanone formation, the entropy of activation is near zero whereas it is about -44 J/K mol for succinimide formation.

Because the IRMPD results clearly show that both succinimide and furanone products are formed, we also evaluated the TCID cross sections including TS parameters for both Fur and Suc

with the difference in threshold energies given by theory. Specifically, the Suc channel was added with a threshold *lower* than that found for Fur by 14 kJ/mol (MP2), lower by 3 kJ/mol (B3P86), and higher by 13 kJ/mol (B3LYP). As shown in Figures 9 and S11, the data are reproduced well in all cases, but the Fur pathway dominates the deamidation products even when the Suc pathway has a lower threshold, again a consequence of the different entropies of reaction. For the B3LYP and B3P86 thresholds, essentially no Suc formation (<2%) is observed at the highest energies (Figure S11), whereas the MP2 relative thresholds predict competition between Fur and Suc formation (Figure 9), consistent with the results from our IRMPD analyses. The threshold found for Suc formation via this approach does not change that for Fur formation, Table 4, and is equivalent to the threshold found by assuming exclusive Suc formation. Experimental evidence that Fur formation is indeed favored comes from the products observed at high energies in Figure 2. Here, both *m/z* 186 and 161 were observed and measured (the two characteristic fragments of $[Fur+H]^+$, Figure S6), whereas only very small amounts of *m/z* 185, 157, and 88 (the characteristic fragments of $[Suc+H]^+$, Figure S6) were observed such that these channels were not monitored for Figure 2.

The model shown in Figure 9 predicts that the Fur product is more prevalent than Suc, in contrast to the results of the isomer population analysis shown in Figure 6. This difference can be attributed to the means used to induce deamidation in the two experiments. TCID corresponds to a single collision depositing a range of energies into the $[AsnSer+H]^+$ species, a method of excitation that tends to yield dissociation channels that are entropically favored (as clearly illustrated in Figure 9 where the smaller Suc cross section has a threshold lower than that for the larger Fur cross section by 14 kJ/mol). In the CID process to produce $[AsnSer+H\text{-}NH_3]^+$ ions for the IRMPD experiments, the ions are formed more slowly by many low-energy collisions with He, which yields dissociation channels that are enthalpically favored. The combination of the two experiments clearly indicates that Suc formation is enthalpically favored, with the MP2 relative energies likely to be most accurate.

Comparable fits can be achieved by loosening the low-frequency modes of $TS_{N\text{-}Fur}$ and $TS_{N\text{-}Suc}$ (by the same magnitude as $TS_{O\text{-}OxaI\text{-}tet\text{-}Nc1}$ was tightened in each case) while holding those for the dehydration channel constant, as demonstrated previously.[16, 18-19] Generally, we believe it is more appropriate to scale the frequencies of the less intense channel, a conclusion that can be checked by comparison of the experimental threshold energies with theoretical predictions. Fitting parameters using scaled $TS_{N\text{-}Fur}$ frequencies are given in Table 4 as an example, where it can be seen that scaling the deamidation channel instead of the minor dehydration channel results in thresholds ~5 kJ/mol higher in energy for both deamidation and dehydration. This increase results in mean absolute deviations from theory that increase by an average of ~4 kJ/mol when this approach is used. Previous thermochemical studies of $[AsnGly+H]^+$, $[AsnAla+H]^+$, and $[AsnVal+H]^+$ also found better agreement between experiment and theory when the less intense competitive channel had its frequencies adjusted.[16, 18-19]

Finally, we checked whether a contribution to the dehydration channel from the minor product, assumed to be $[DKP+H]^+$, made any difference in the analyses. Theory places the rate-limiting step for DKP formation, $TS_{O\text{-}DKP}$ in Figure S9, as 7 – 16 kJ/mol above $TS_{O\text{-}OxaI\text{-}tet\text{-}Nc1}$ (Figure 7), but the former TS is looser ($\Delta S^{\dagger}_{1000}$ = -55 J/K mol compared to -83 J/K mol for OxaI formation). As a consequence, if the formation of DKP is assumed to lie ~15 kJ/mol higher than OxaI formation (as per B3P86 and MP2 results), the threshold behavior is dominated by formation of OxaI (although the threshold shifts upward by 1 – 2 kJ/mol). If the difference in thresholds is only 7 kJ/mol (as predicted by B3LYP), then the contribution of both channels in the threshold region is comparable and the threshold shifts up by 5 – 6 kJ/mol. As noted above and confirmed by comparison with theory below, the MP2 energetics are believed to be most reliable in this system.

Conversion of Thermodynamic Parameters from 0 to 298K. Table 5 provides the conversion from 0 K thresholds to 298 K enthalpies and Gibbs energies. This conversion is accomplished using the rigid rotor/harmonic oscillator approximations with rotational constants

and vibrational frequencies calculated at the B3LYP/6-311+G(d,p) level. Uncertainties given in Table 5 are determined by scaling the vibrational frequencies by ± 10%.

Discussion

Thresholds found for deamidation via both $[Suc+H]^+$ and $[Fur+H]^+$ formation (modeling both contributions to the deamidation channel concomitantly) were found to be 131 ± 12 and 145 ± 12 kJ/mol, respectively, and are compared to theoretical predictions in Table 6. These thresholds are found to lie within experimental uncertainty of the MP2 predicted values of 130 and 144 kJ/mol, respectively, which reproduce the experimental difference between them exactly. B3P86 predicts a similar threshold for $[Fur+H]^+$ formation (145 kJ/mol), but a threshold much higher than experiment for $[Suc+H]^+$ formation. The B3LYP predicted values (151 kJ/mol for $[Suc+H]^+$ and 138 kJ/mol for $[Fur+H]^+$) exhibit the largest difference from experiment, and also would predict that formation of $[Fur+H]^+$ would be dominant over $[Suc+H]^+$. In contrast to these latter conclusions, slow collisional heating of $[AsnSer+H]^+$ yields more $[Suc+H]^+$ (70%) than $[Fur+H]^+$ (30%), suggesting the former has the lower threshold energy. Overall, the MP2 level of theory yields thermochemistry in good agreement with experiment and also is the only level of theory that predicts reasonable competition between formation of both furanone and succinimide, Figure 9.

When the dehydration channel is modeled in competition with both deamidation channels, an experimental threshold of 104 ± 9 kJ/mol is found (as also found if deamidation forms $[Fur+H]^+$ exclusively). Alternatively, modeling with parameters for exclusive $[Suc+H]^+$ formation leads to a threshold energy of 102 ± 8 kJ/mol. Including the possibility of $[DKP+H]^+$ formation would shift these values up about 1 kJ/mol. The average of all possible interpretations yields a threshold of 104 ± 10 kJ/mol as our best threshold value for dehydration. This threshold energy is reproduced well by the MP2 predicted energy for $[OxaI+H]^+$ formation of 100 kJ/mol, respectively, whereas B3LYP and B3P86 suggests reaction energies about 1 standard deviation above or below. Overall, calculated mean absolute deviations (MADs, Table 6) from experiment suggest that there is good

agreement with all levels of theory. MP2 resulted in the lowest MAD (2 ± 2 kJ/mol), with B3P86 and B3LYP having 8 ± 7 and 12 ± 7 kJ/mol, respectively.

Our groups have previously evaluated the deamidation processes of $[AsnGly+H]^+$, $[AsnAla+H]^+$, $[AsnVal+H]^+$, and $[AsnThr+H]^+$ [16-20] in order to determine the specific interactions that hinder or accelerate the deamidation reaction. At threshold energies, $[AsnGly+H]^+$ and $[AsnThr+H]^+$ favor succinimide formation,[16, 20] whereas furanone formation is observed at threshold energies in the larger aliphatic systems (an effect that appears to directly correlate with an *n+1* side-chain steric contribution, where Asn defines *n*).[18-19] Among the aliphatic *n+1* systems, DFT methods predict that reaction barriers for succinimide formation increase by roughly 10 kJ/mol as the steric contribution of the *n+1* side chain increases (Gly to Ala to Val). MP2 predicts smaller increases in theoretical reaction barriers (averaging 6 kJ/mol). Theoretical reaction barriers for the alternative furanone formation are minimally affected by steric effects, as ring formation is more localized to the N-terminus such that side-chain steric effects are largely negated via this pathway (see Figure 4). Experimentally, however, we do observe a small increase in experimental threshold values as the steric contribution increases, where thresholds found in the Ala and Val systems (leading to Fur) were found to be 123 ± 5 and 129 ± 5 kJ/mol, respectively.

Those experimental results are paralleled in the hydroxyl-containing systems, $[AsnSer+H]^+$ and $[AsnThr+H]^+$. The threshold found for succinimide formation in the current work is 131 ± 12 kJ/mol, whereas in the larger $[AsnThr+H]^+$ system the threshold was determined to be 142 ± 6 kJ/mol.[20] Interestingly, our theoretical results do not predict this difference in energetics (although this difference is in line with the increase in succinimide reaction barriers found for the aliphatic systems described above). The MP2 predicted reaction barrier for succinimide formation in the larger $[AsnThr+H]^+$ system is only 3 kJ/mol higher than the analogous pathway in the current work. DFT methods predict nearly isoenergetic reaction barriers. From a qualitative point of view, the efficiency of deamidation in the current $[AsnSer+H]^+$ system may explain the difference in cross section behavior observed. Here, at the highest collision energies measured, deamidation is the dominant pathway (although it includes contributions from both succinimide and furanone

pathways). In the previous (and more sterically strained) $[AsnThr+H]^+$ system, dehydration dominated the deamidation cross section (resulting from exclusive formation of the succinimide product) at all collision energies studied. This deamidation acceleration for the Ser residue compared to Thr is consistent with the relative deamidation half-times of GlyYyyAsnXxxGly pentapeptides noted above.[15]

Bifurcating pathways are also observed for the dehydration channel. Consistent with a more extensive examination of dipeptides containing hydroxyl side chains,[22] the main pathway for dehydration of $[AsnSer+H]^+$ occurs not by loss of the terminal hydroxyl group (which would form an oxazolone), but rather involves the hydroxyl side chain. Theory indicates that this mechanism passes through a tetrahedral intermediate (Figure 7) and eventually loses water containing the peptide-bond O^1 oxygen, rather than the side-chain oxygen (O^{s2}). Comparison with the comparable pathway elucidated for dehydration of $[GlySer+H]^+$ [22] indicates that the carboxamide side chain lowers the overall energy for this process. An alternative pathway for dehydration, which IR spectra suggests is either $[MKP+H]^+$ or $[DKP+H]^+$, is also available. Here, theory indicates that formation of DKP is more likely and limited by a transition state in which the six-membered ring is closed (forming a tetrahedral gem-diol intermediate, INT(O-DKP[N^1]c), Figure S10). Prior cis-trans isomerization of the peptide bond, which is required for either MKP or DKP formation, does not appear to be restrictive. Here, the water lost contains O^2 (the terminal carbonyl oxygen), although loss of O^3 (the terminal hydroxyl oxygen) also seems feasible. Clearly, labeling experiments would be of interest to verify these theoretical predictions.

Conclusions

The decomposition of $[AsnSer+H]^+$ was studied by measuring kinetic energy dependent thresholds for collision-induced dissociation with Xe using a GIBMS with the dominant processes observed being deamidation and dehydration. The product species formed in these pathways were further evaluated using IRMPD action spectroscopy. This combination of techniques allows for

the structural identification of $[AsnSer+H]^+$, $[AsnSer+H–NH_3]^+$, and $[AsnSer+H–H_2O]^+$ as well as the energetic analysis of the associated reaction mechanisms.

Bifurcating pathways were observed such that deamidation leads to $[Suc+H]^+$ and $[Fur+H]^+$ formation, with the former constituting about 70% of the ion population formed by CID in the quadrupole ion trap that is also used for the IRMPD experiments. This is consistent with theoretical findings that suggest similar rate-limiting energies for $[Suc+H]^+$ (130 – 151 kJ/mol) and $[Fur+H]^+$ formation (138 – 144 kJ/mol), with the former process dominating when collisional activation occurs via slow-heating but the latter process being more prevalent in single-collision TCID because of entropic effects. TCID experiments conclude that $[Suc+H]^+$ and $[Fur+H]^+$ formation are characterized by energy onsets of 131 ± 12 and 145 ± 12 kJ/mol, respectively (whether modeled in isolation or when both contributions to the deamidation channel are modeled concomitantly). Because the adverse affects of protein deamidation are largely a consequence of hydration of the succinimide to form an iso-aspartyl residue, the prevalence of $[Suc+H]^+$ formation observed here is relevant to the physiological process. For dehydration, bifurcating pathways were also observed with oxazaline $[OxaI+H]^+$ formation dominating and characterized by a threshold energy of 104 ± 10 kJ/mol (when considering threshold values from all modeling approaches). In addition, theory suggests that a competitive pathway for formation of a diketopiperazine product is available, and the $[DKP+H]^+$ species has a predicted IR spectrum consistent with the minor constituent of the dehydration products.

We can also compare the present results with those for deamidation of other dipeptides. Direct comparison to $[AsnThr+H]^+$ elucidates steric effects on OH-functionalized $n+1$ side chains. Here, we find that deamidation (leading to succinimide formation) from the current $[AsnSer+H]^+$ system, 131 ± 12 kJ/mol, is ~10 kJ/mol lower in energy that the analogous reaction from $[AsnThr+H]^+$. This deamidation acceleration is slightly larger than the difference in threshold energies for deamidation in the $[AsnAla+H]^+$ and $[AsnVal+H]^+$ studies (although furanone formation was the dominant deamidation pathway observed in those analyses). Notably, additional factors (such as solvation by water and peptide chain length) may play integral roles in condensed-

phase Asn deamidation. Additional studies probing these aspects of deamidation are certainly warranted and are currently being conducted in our laboratories.

Acknowledgment. We gratefully acknowledge the *Nederlandse Organisatie voor Wetenschappelijk Onderzoek* (NWO) for the support of the FELIX Laboratory and for funding for this specific project through VICI grant 724.011.002. Financial support for this work was provided by the National Science Foundation, Grant CHE- 1954142. The skillful assistance of the FELIX staff is gratefully acknowledged. In addition, a grant of computer time from the Center of High Performance Computing at the University of Utah is greatly appreciated. The authors also thank the reviewers for several helpful comments.

Supporting Information Available: Additional figures include comparison of the experimental $[AsnSer+H-NH_3]^+$ spectra against computed spectra for select $[DKM+H]^+$ and $[Suc+H]^+$ structures, structures of alternate $[Suc+H]^+$ isomers, mass spectrum of the IRMPD induced fragmentation of $[AsnSer+H–NH_3]^+$ at two frequencies, and alternate models of the TCID cross sections, structures calculated along reaction coordinates for dehydration leading to oxazoline, oxazolone, and diketopiperazine formation in addition to the sequential losses of NH_3 from $[Suc+H]^+$ and $[Fur+H]^+$ as well as H_2O from $[Suc+H]^+$.

References

1. Stephenson, R. C.; Clarke, S., Succinimde Formation from Aspartyl and Asparaginyl Peptides as a Model for the Spontaneous Degradation of Proteins. *J. Biol. Chem.* **1989,** *264*, 6164-6170.
2. Geiger, T.; Clarke, S., Deamidation, isomerization, and racemization at asparaginyl and aspartyl residues in peptides. Succinimide-linked reactions that contribute to protein degradation. *J. Biol. Chem.* **1987,** *262*, 785-794.
3. Robinson, A. B.; McKerrow, J. H.; Legaz, M., Sequence dependent deamidation rates for model peptides of cytochrome C. *Int. J. Pept. Protein Res.* **1974,** *6*, 31-35.
4. Fujii, N.; Takata, T.; Fujii, N.; Aki, K., Isomerization of aspartyl residues in crystallins and its influence upon cataract. *Biochim. Biophys. Acta* **2016,** *1860*, 183-191.

5. Zomber, G.; Reuveny, S.; Garti, N.; Shafferman, A.; Elhanany, E., Effects of spontaneous deamidation on the cytotoxic activity of the Bacillus anthracis protective antigen. *J. Biol. Chem.* **2005,** *280*, 39897-39906.
6. Nilsson, M. R.; Driscoll, M.; Raleigh, D. P., Low Levels of Asparagine Deamidation Can Have a Dramatic Effect on Aggregation of Amyloidogenic Peptides: Implications for the Study of Amyloid Formation. *Protein Sci.* **2002,** *11*, 342-349.
7. Hains, P. G.; Truscott, R. J., Age-dependent deamidation of lifelong proteins in the human lens. *Investigative ophthalmology & visual science* **2010,** *51*, 3107-3114.
8. Robinson, N. E.; Robinson, A. B., *Molecular Clocks: Deamidation of Asparaginyl and Glutaminyl Residues in Peptides and Proteins*. Althouse Press: Cave Junction, OR, 2004.
9. Roher, A. E.; Lowenson, J. D.; Clarke, S.; Wolkow, C.; Wang, R.; Cotter, R. J.; Reardon, I. M.; Zürcher-Neely, H. A.; Heinrikson, R. L.; Ball, M. J.; Greenberg, B. D., Structural alterations in the peptide backbone of beta-amyloid core protein may account for its deposition and stability in Alzheimer's disease. *J. Biol. Chem.* **1993,** *268*, 3072-3083.
10. Kim, E.; Lowenson, J. D.; MacLaren, D. C.; Clarke, S.; Young, S. G., Deficiency of a protein-repair enzyme results in the accumulation of altered proteins, retardation of growth, and fatal seizures in mice. *Proc. Natl. Acad. Sci. U. S. A.* **1997,** *94*, 6132-6137.
11. Shimizu, T.; Watanabe, A.; Ogawara, M.; Mori, H.; Shirasawa, T., Isoaspartate formation and neurodegeneration in Alzheimer's disease. *Arch. Biochem. Biophys.* **2000,** *381*, 225-234.
12. Cournoyer, J. J.; Pittman, J. L.; Ivleva, V. B.; Fallows, E.; Waskell, L.; Costello, C. E.; O'Connor, P. B., Deamidation: Differentiation of aspartyl from isoaspartyl products in peptides by electron capture dissociation. *Protein Sci.* **2005,** *14*, 452-463.
13. Sargaeva, N. P.; Lin, C.; O'Connor, P. B., Identification of Aspartic and Isoaspartic Acid Residues in Amyloid β Peptides, Including Aβ1−42, Using Electron−Ion Reactions. *Anal. Chem.* **2009,** *81*, 9778-9786.
14. Schiffter, H. A., Medical Biotechnology and Healthcare. In *Comprehensive Biotechnology (2nd Edition)*, Moo-Young, M., Ed. Elsevier: 2011.
15. Robinson, N. E.; Robinson, A. B., Deamidation of Human Proteins. *Proc. Natl. Acad. Sci.* **2001,** *98*, 12409-12413.
16. Boles, G. C.; Wu, R. R.; Rodgers, M. T.; Armentrout, P. B., Thermodynamics and Mechanisms of Protonated Asparaginyl-Glycine Decomposition. *J. Phys. Chem. B* **2016,** *120*, 6525−6545.
17. Kempkes, L. J. M.; Martens, J.; Grzetic, J.; Berden, G.; Oomens, J., Deamidation Reactions of Asparagine- and Glutamine-Containing Dipeptides Investigated by Ion Spectroscopy. *J. Am. Soc. Mass Spectrom.* **2016,** *11*, 1855-1869.
18. Boles, G. C.; Wu, R. R.; Rodgers, M. T.; Armentrout, P. B., Protonated Asparaginyl-Alanine Decomposition: a TCID, SORI-CID, and Computational Analysis. *J. Am. Soc. Mass Spectrom.* **2018,** *29*, 2341-2359.
19. Kempkes, L. J. M.; Boles, G. C.; Martens, J.; Berden, G.; Armentrout, P. B.; Oomens, J., Deamidation of Protonated Asparagine–Valine Investigated by a Combined Spectroscopic, Guided Ion Beam, and Theoretical Study. *J. Phys. Chem. A* **2018,** *122*, 2424-2436.
20. Boles, G. C.; Kempkes, L. J. M.; Martens, J.; Berden, G.; Oomens, J.; Armentrout, P. B., Ion Spectroscopy and Guided Ion Beam Studies of Protonated Asparaginyl-Threonine Decomposition: Influence of a Hydroxyl Containing C-Terminal Residue on Deamidation Processes. *Int. J. Mass Spectrom.* **2019,** *442*, 64-82.

21. Capasso, S.; Mazzarella, L.; Sica, F.; Zagari, A.; Salvadore, S., Kinetics and Mechanism of Succinimide Ring Formation in the Deamidation Process of Asparagine Residues. *J. Chem. Soc. Perkins Trans. 2* **1993**, 679-682.
22. Oomens, J.; Kempkes, L. J. M.; Geurts, T. P. J.; van Dijk, L.; Martens, J.; Berden, G.; Armentrout, P. B., Water Loss from Protonated XxxSer and XxxThr Dipeptides Gives Oxazoline—Not Oxazolone—Product Ions. *J. Am. Soc. Mass Spectrom.* **2020,** *31*, 2111-2123.
23. Oepts, D.; van der Meer, A. F. G.; van Amersfoort, P. W., The Free-Electron-Laser User Facility FELIX. *Infrared Phys. Technol.* **1995,** *36*, 297-308.
24. Martens, J.; Berden, G.; Gebhardt, C. R.; Oomens, J., Infrared ion spectroscopy in a modified quadrupole ion trap mass spectrometer at the FELIX free electron laser laboratory. *Rev. Sci. Instrum.* **2016,** *87*, 103108.
25. Ervin, K. M.; Armentrout, P. B., Translational Energy Dependence of $Ar^+ + XY \rightarrow ArX^+ + Y$ ($XY = H_2$, D_2, HD) from Thermal to 30 eV c.m. *J. Chem. Phys.* **1985,** *83*, 166-189.
26. Muntean, F.; Armentrout, P. B., Guided Ion Beam Study of Collision-Induced Dissociation Dynamics: Integral and Differential Cross Sections. *J. Chem. Phys.* **2001,** *115*, 1213-1228.
27. Armentrout, P. B., Not Just a Structural Tool: The Use of Guided Ion Beam Tandem Mass Spectrometry to Determine Thermochemistry. *J. Am. Soc. Mass Spectrom.* **2002,** *13*, 419-434.
28. Moision, R. M.; Armentrout, P. B., An Electrospray Ionization Source for Thermochemical Investigation with the Guided Ion Beam Mass Spectrometer. *J. Am. Soc. Mass Spectrom.* **2007,** *18*, 1124-1134.
29. Kim, T.; Tolmachev, A. V.; Harkewicz, R.; Prior, D. C.; Anderson, G.; Udseth, H. R.; Smith, R. D.; Bailey, T. H.; Rakov, S.; Futrell, J. H., Design and Implementation of a New Electrodynamic Ion Funnel. *Anal. Chem* **2000,** *72*, 2247-2255.
30. Ye, S. J.; Armentrout, P. B., Absolute Thermodynamic Measurements of Alkali Metal Cation Interactions with a Simple Dipeptide and Tripeptide. *J. Phys. Chem. A* **2008,** *112*, 3587-3596.
31. Carl, D. R.; Chatterjee, B. K.; Armentrout, P. B., Threshold Collision-induced Dissociation of $Sr^{2+}(H_2O)_x$ Complexes ($x = 1 – 6$): An Experimental and Theoretical Investigation of the Complete Inner Shell Hydration Energies of Sr^{2+}. *J. Chem. Phys.* **2010,** *132*, 044303.
32. Carpenter, J. E.; McNary, C. P.; Furin, A.; Sweeney, A. F.; Armentrout, P. B., How Hot are Your Ions Really? A Threshold Collision-Induced Dissociation Study of Substituted Benzylpyridinium "Thermometer" Ions. *J. Am. Soc. Mass Spectrom.* **2017,** *28*, 1876-1888.
33. Gerlich, D., Inhomogeneous rf Fields: A Versatile Tool for the Study of Processes with Slow Ions. In *Adv. Chem. Phys.*, Ng, C.-Y.; Baer, M., Eds. 1992; Vol. 82, pp 1-176.
34. Aristov, N.; Armentrout, P. B., Collision-Induced Dissociation of Vanadium Monoxide Ion. *J. Phys. Chem.* **1986,** *90*, 5135-5140.
35. Daly, N. R., Scintillation Type Mass Spectrometer Ion Detector. *Rev. Sci. Instrum.* **1960,** *31*, 264-267.
36. Beyer, T. S.; Swinehart, D. F., Number of Multiply-Restricted Partitions. *Commun. ACM* **1973,** *16*, 379.
37. Stein, S. E.; Rabinovich, B. S., On the Use of Exact State Counting Methods in RRKM Rate Calculations. *Chem. Phys. Lett.* **1977,** *49*, 183-188.
38. Gilbert, R. G.; Smith, S. C., *Theory of Unimolecular and Recombination Reactions*. Blackwell Scientific: London, 1990.
39. Robinson, P. J.; Holbrook, K. A., *Unimolecular Reactions*. Wiley Interscience: New York, 1972.

40. Rodgers, M. T.; Ervin, K. M.; Armentrout, P. B., Statistical Modeling of Collision-Induced Dissociation Thresholds. *J. Chem. Phys.* **1997,** *106*, 4499-4508.
41. Rodgers, M. T.; Armentrout, P. B., Statistical Modeling of Competitive Threshold Collision-Induced Dissociation. *J. Chem. Phys.* **1998,** *109*, 1787-1800.
42. Lifshitz, C.; Wu, R. L. C.; Tiernan, T. O.; Terwilliger, D. T., Negative Ion-molecule Reactions of Ozone and Their Implications on the Thermochemistry of O_3^-. *J. Chem. Phys.* **1978,** *68*, 247-260.
43. Frisch, M. J.; Trucks, G. W.; Schlegel, H. B.; Scuseria, G. E.; Robb, M. A.; Cheeseman, J. R.; Scalmani, G.; Barone, V.; Mennucci, B.; Petersson, G. A.; Nakatsuji, H.; Caricato, M.; Li, X.; Hratchian, H. P.; Izmaylov, A. F.; Bloino, J.; Zheng, G.; Sonnenberg, J. L.; Hada, M.; Ehara, M.; Toyota, K.; Fukuda, R.; Hasegawa, J.; Ishida, M.; Nakajima, T.; Honda, Y.; Kitao, O.; Nakai, H.; Vreven, T.; Montgomery Jr., J. A.; Peralta, J. E.; Ogliaro, F.; Bearpark, M. J.; Heyd, J.; Brothers, E. N.; Kudin, K. N.; Staroverov, V. N.; Kobayashi, R.; Normand, J.; Raghavachari, K.; Rendell, A. P.; Burant, J. C.; Iyengar, S. S.; Tomasi, J.; Cossi, M.; Rega, N.; Millam, N. J.; Klene, M.; Knox, J. E.; Cross, J. B.; Bakken, V.; Adamo, C.; Jaramillo, J.; Gomperts, R.; Stratmann, R. E.; Yazyev, O.; Austin, A. J.; Cammi, R.; Pomelli, C.; Ochterski, J. W.; Martin, R. L.; Morokuma, K.; Zakrzewski, V. G.; Voth, G. A.; Salvador, P.; Dannenberg, J. J.; Dapprich, S.; Daniels, A. D.; Farkas, Ö.; Foresman, J. B.; Ortiz, J. V.; Cioslowski, J.; Fox, D. J. *Gaussian 09, Revision D.01* Gaussian, Inc.: Wallingford, CT, USA, 2009.
44. Kesharwani, M. K.; Brauer, B.; Martin, J. M. L., Frequency and Zero-Point Vibrational Energy Scale Factors for Double-Hybrid Density Functionals (and Other Selected Methods): Can Anharmonic Force Fields Be Avoided? *J. Phys. Chem. A* **2015,** *119*, 1701-1714.
45. Prell, J. S.; Chang, T. M.; Biles, J. A.; Berden, G.; Oomens, J.; Williams, E. R., Isomer Population Analysis of Gaseous Ions From Infrared Multiple Photon Dissociation Kinetics. *J. Phys. Chem. A* **2011,** *115*, 2745-2751.
46. Munshi, M. U.; Martens, J.; Berden, G.; Oomens, J., Protoisomerization of Indigo and Isoindigo Dyes Confirmed by Gas-Phase Infrared Ion Spectroscopy. *J. Phys. Chem. A* **2019,** *123*, 8226-8233.
47. Corinti, D.; De Petris, A.; Coletti, C.; Re, N.; Chiavarino, B.; Crestoni, M. E.; Fornarini, S., Cisplatin Primary Complex with l-Histidine Target Revealed by IR Multiple Photon Dissociation (IRMPD) Spectroscopy. *ChemPhysChem* **2017,** *18*, 318-325.
48. Paciotti, R.; Corinti, D.; De Petris, A.; Ciavardini, A.; Piccirillo, S.; Coletti, C.; Re, N.; Maitre, P.; Bellina, B.; Barran, P.; Chiavarino, B.; Elisa Crestoni, M.; Fornarini, S., Cisplatin and transplatin interaction with methionine: bonding motifs assayed by vibrational spectroscopy in the isolated ionic complexes. *Phys. Chem. Chem. Phys.* **2017,** *19*, 26697-26707.
49. Perkins, B. R.; Chamot-Rooke, J.; Yoon, S. H.; Gucinski, A. C.; Somogyi, A.; Wysocki, V. H., Evidence of Diketopiperazine and Oxazolone Structures for HA b_2^+ Ion. *J. Am. Chem. Soc.* **2009,** *131*, 17528-17529.
50. Armentrout, P. B.; Clark, A. A., The Simplest b_2^+ Ion: Determining Its Structure from Its Energetics by a Direct Comparison of the Threshold Collision-induced Dissociation of Protonated Oxazolone and Diketopiperazine. *Int. J. Mass Spectrom.* **2012,** *316-318*, 182–191.
51. Wang, D.; Gulyuz, K.; Stedwell, C. N.; Yu, L.; Polfer, N. C., Effect of phenol and acidic side chains on the protonation sites of b_2 ions confirmed by IRMPD spectroscopy. *Int. J. Mass Spectrom.* **2012,** *330-332*, 144-151.
52. Grzetic, J.; Oomens, J., Spectroscopic Evidence for an Oxazolone Structure in Anionic b-Type Peptide Fragments. *J. Am. Soc. Mass Spectrom.* **2012,** *23*, 290-300.

53. Kempkes, L. J. M.; Martens, J.; Berden, G.; Oomens, J., Dehydration reactions of protonated dipeptides containing asparagine or glutamine investigated by infrared ion spectroscopy. *Int. J. Mass Spectrom.* **2018,** *429*, 90-100.
54. Reid, G. E.; Simpson, R. J.; O'Hair, R. A. J., Leaving group and gas phase neighboring group effects in the side chain losses from protonated serine and its derivatives. *J. Am. Soc. Mass Spectrom.* **2000,** *11*, 1047-1060.
55. Heaton, A. L.; Armentrout, P. B., Thermodynamics and Mechanism of Protonated Asparagine Decomposition. *J. Am. Soc. Mass Spectrom.* **2009,** *20*, 852-866.

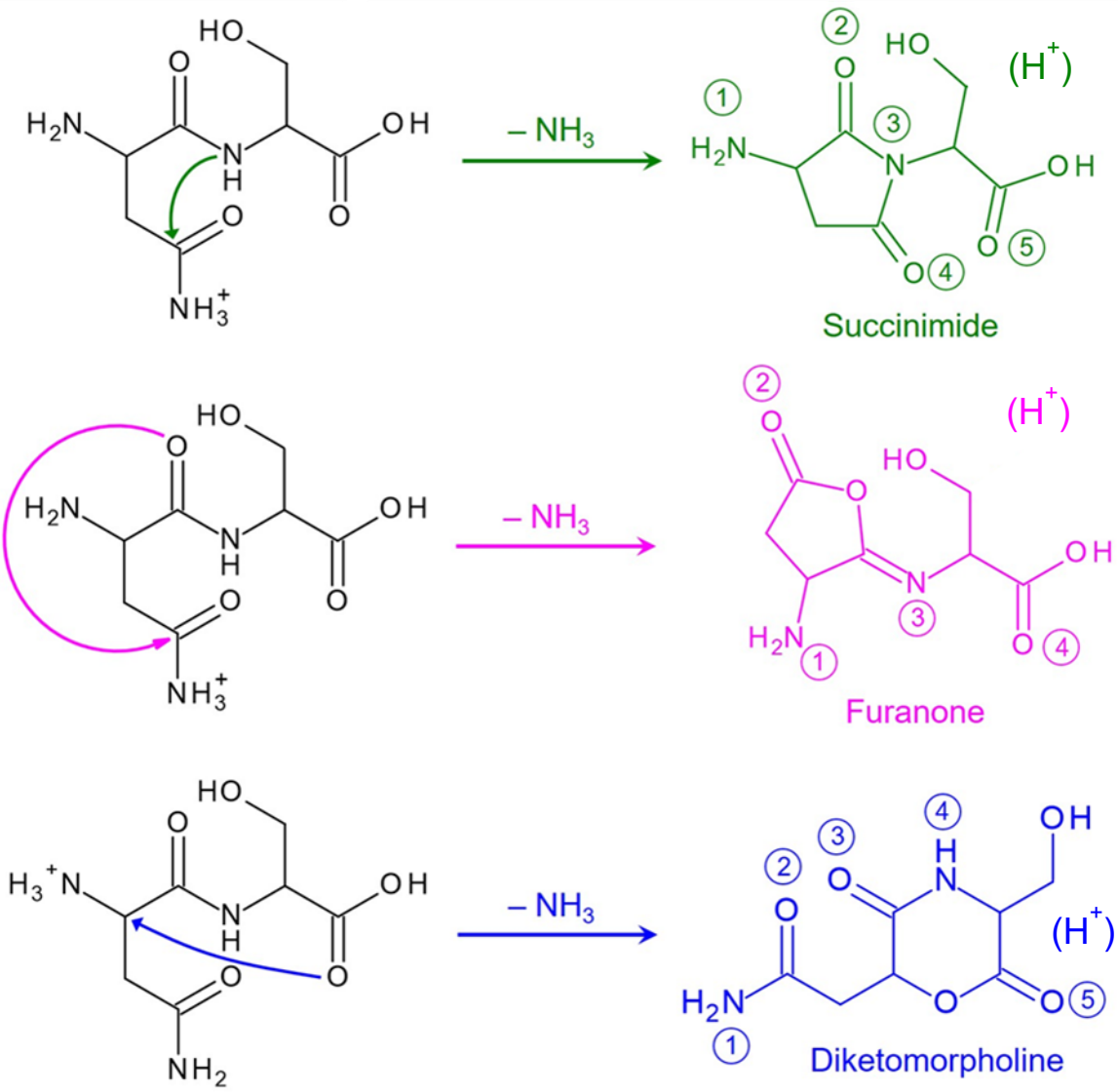

Scheme 1. Possible reaction mechanisms for the deamidation of $[AsnSer+H]^+$. The curved arrows indicate nucleophilic attack inducing the expulsion of a neutral NH_3. The numbered atoms in the products indicate the protonation sites considered. In the main text, the $[AsnSer+H-NH_3]^+$ products are labeled as **$[name+H]^+$-x.y** where "name" is Suc, Fur, or DKM, x indicates the protonation site shown here, and y indicates the specific conformer (in order of lowest energy starting at 1).

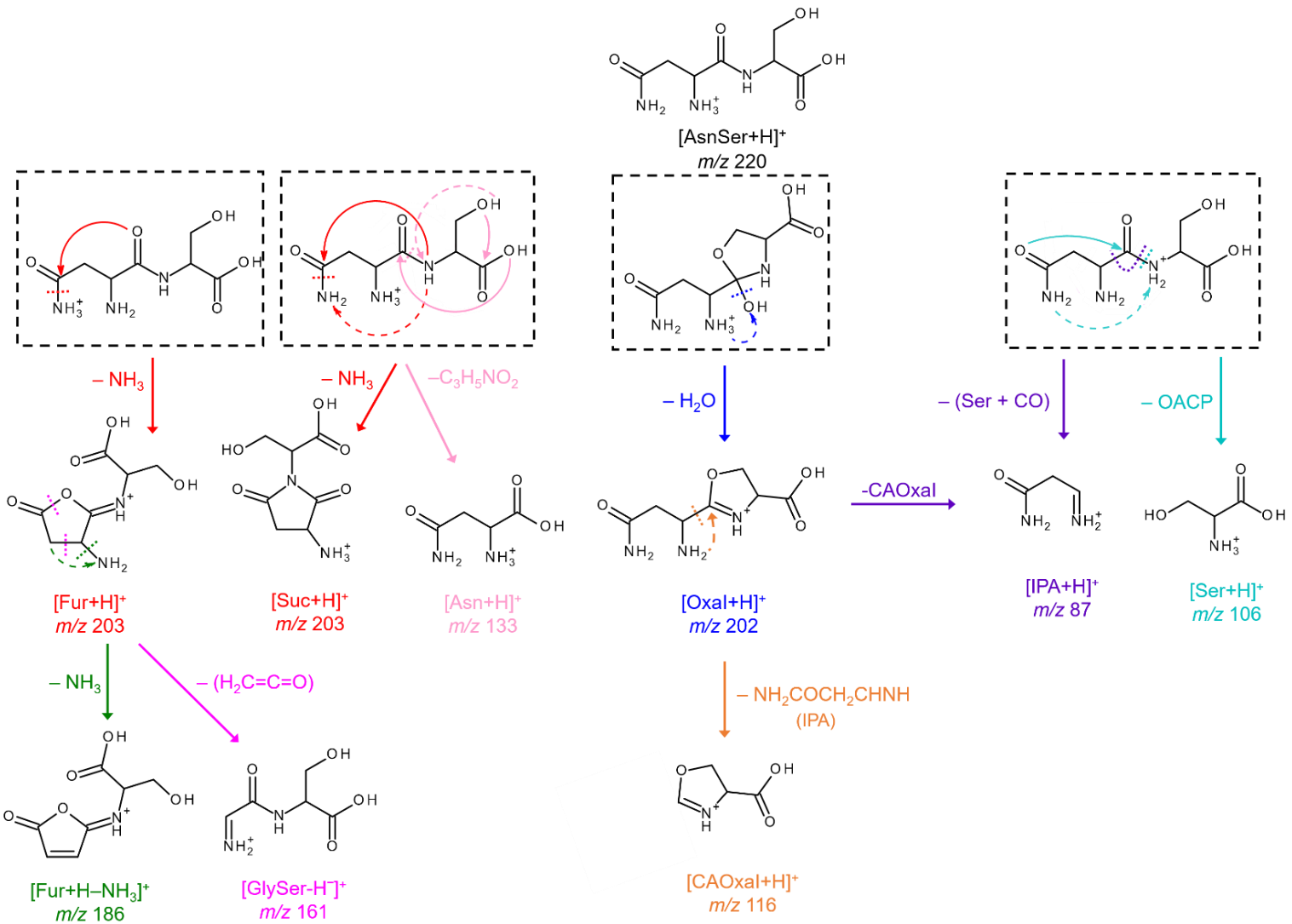

Scheme 2. Major decomposition reaction pathways for $[AsnSer+H]^+$ observed in TCID studies under unit mass-resolution conditions. Numbers indicate mass-to-charge ratios and are given along with nomenclature used in the text. Dashed lines indicate proton movement, dotted lines indicate bond cleavages, solid lines indicate bond formation, and lines are color-coded to the resultant reaction.

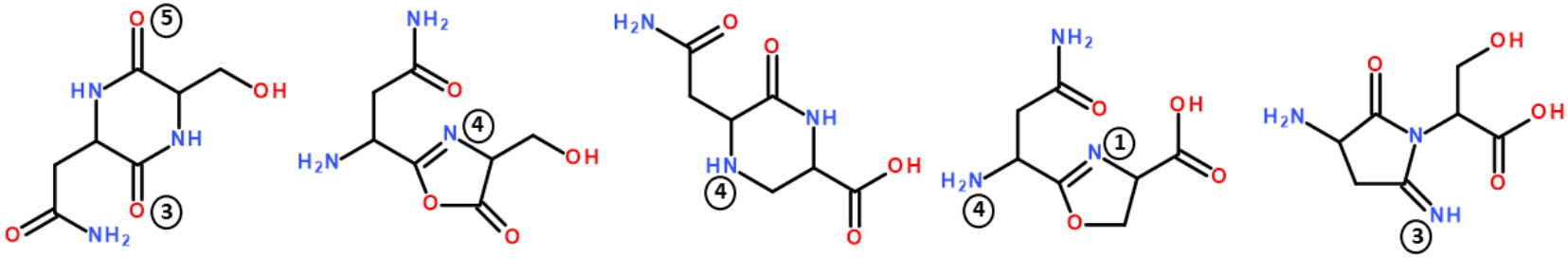

Scheme 3. Possible reaction products from dehydration of $[AsnSer+H]^+$. The numbered atoms in the products indicate the protonation sites discussed in the text. In the main text, the $[AsnSer+H-H_2O]^+$ products are labeled as **[name+H]$^+$-x.y.z** where "name" and x are DKP and 1, OxaO and 2, MKP and 3, OxaI and 4, or Pyr and 5, y indicates the protonation site shown here, and z indicates the specific conformer (in order of lowest energy starting at 1).

Table 1. Relative Enthalpies (0 K) and Gibbs Energies (298 K) in kJ/mol for Possible $[AsnSer+H–NH_3]^+$ Product Structures[a]

	$[Suc+H]^+$		$[Fur+H]^+$		$[DKM+H]^+$	
Protonation Site	B3LYP	MP2	B3LYP	MP2	B3LYP	MP2
1	15 (17)	0 (0)	112 (108)	111 (105)	78 (77)	93 (89)
2	22 (19)	20 (16)	[b]	[b]	0 (0)	27 (25)
3	137 (133)	122 (116)	31 (26)	41 (34)	76 (75)	94 (91)
4	13 (11)	13 (10)	133 (127)	153 (146)	133 (126)	149 (140)
5	61 (60)	68 (65)			69 (66)	97 (91)

[a] Calculations performed at the stated level of theory using a 6-311+G(2d,2p) basis set with geometries and vibrational frequencies calculated at B3LYP/6-311+G(d,p) level for protonation sites illustrated in Scheme 1. Gibbs energies in parentheses.

[b] Protonation at site 2, Scheme 1, leads to opening of the furanone ring.

Table 2. Relative Enthalpies (0 K) and Gibbs Energies (298 K) in kJ/mol of Possible Succinimide and Furanone Deamidation Products of $[AsnSer+H]^+$ [a]

Species	B3LYP	B3P86	MP2(full)
$[Suc+H]^+$-4.1	*110.9 (75.6)* [b]	*114.5 (79.2)* [b]	*116.3 (78.3)* [b]
	0.0 (0.0)	0.0 (0.0)	13.3 (11.5)
$[Suc+H]^+$-4.2	1.6 (1.8)	1.5 (1.6)	13.0 (11.4)
$[Suc+H]^+$-1.1	2.3 (5.8)	0.9 (4.5)	0.0 (1.7)
$[Suc+H]^+$-1.2	3.8 (4.9)	4.0 (5.2)	0.6 (0.0)
$[Suc+H]^+$-1.3	5.4 (2.4)	8.1 (5.1)	8.7 (3.9)
$[Suc+H]^+$-1.4	5.9 (3.0)	8.5 (5.6)	8.9 (4.2)
$[Suc+H]^+$-1.5	6.9 (6.7)	7.2 (6.9)	4.7 (2.6)
$[Suc+H]^+$-4.3	7.2 (6.5)	6.4 (5.7)	19.1 (16.6)
$[Suc+H]^+$-4.4	8.2 (8.3)	8.1 (8.2)	21.2 (19.5)
$[Suc+H]^+$-4.5	8.6 (7.5)	7.7 (6.6)	24.7 (21.9)
$[Suc+H]^+$-2.1	9.0 (7.3)	8.1 (6.4)	24.5 (21.1)
$[Suc+H]^+$-2.2	9.2 (8.6)	8.5 (7.9)	20.3 (17.8)
$[Suc+H]^+$-1.6	9.5 (14.3)	5.0 (9.7)	8.7 (11.6)
$[Suc+H]^+$-2.3	16.8 (15.1)	15.9 (14.2)	34.1 (30.7)
$[Fur+H]^+$-3.1	*129.0 (90.2)* [b]	*139.8 (101.0)* [b]	*144.2 (102.7)* [b]
	18.1 (14.6)	25.3 (21.8)	41.2 (35.9)
$[Fur+H]^+$-3.2	36.3 (33.0)	43.3 (40.0)	65.5 (60.4)
$[Fur+H]^+$-3.3	39.0 (33.4)	46.7 (41.1)	67.0 (59.6)
$[Fur+H]^+$-3.4	46.3 (40.0)	53.9 (47.6)	73.7 (65.6)

[a] Calculations performed at the stated level of theory using a 6-311+G(2d,2p) basis set with geometries and vibrational frequencies calculated at B3LYP/6-311+G(d,p) level for protonation sites illustrated in Scheme 1. Gibbs energies in parentheses.

[b] Values in italics indicate energies relative to the $[AsnSer+H]^+$-1 GS including the NH_3 product.

Table 3. Relative Enthalpies (0 K) and Gibbs Energies (298 K) in kJ/mol of Possible Dehydration Products of $[AsnSer+H]^+$ [a]

Species	B3LYP	B3P86	MP2(full)
$[MKP+H]^+$-3.4.1	*17.8 (-15.8)*[b] 0.0 (0.0)	*16.5 (-17.1)*[b] 0.0 (0.0)	*15.6 (-20.7)*[b] 0.0 (0.0)
$[MKP+H]^+$-3.4.2	31.9 (30.0)	33.2 (31.3)	34.8 (32.8)
$[DKP+H]^+$-1.5.1	36.0 (35.6)	37.3 (36.9)	48.7 (51.0)
$[DKP+H]^+$-1.3.1	36.8 (36.0)	35.7 (34.9)	56.0 (57.9)
$[DKP+H]^+$-1.5.2	38.3 (37.5)	40.1 (39.3)	51.5 (53.3)
$[OxaI+H]^+$-4.1.1	41.2 (37.3)	47.7 (43.7)	51.8 (47.9)
$[OxaI+H]^+$-4.1.2	41.6 (37.3)	48.3 (44.0)	53.2 (48.9)
$[DKP+H]^+$-1.5.3	46.8 (47.2)	49.1 (49.6)	50.6 (53.7)
$[Pyr+H]^+$-5.3.1	47.7 (46.5)	52.0 (50.7)	43.6 (42.3)
$[Pyr+H]^+$-5.3.2	54.4 (53.2)	57.5 (56.3)	50.7 (49.4)
$[OxaI+H]^+$-4.4.1	56.0 (50.7)	59.7 (54.3)	62.0 (56.7)
$[OxaI+H]^+$-4.1.3	61.5 (53.2)	69.0 (60.7)	81.5 (73.2)
$[DKP+H]^+$-1.5.4	64.7 (61.8)	67.8 (64.9)	77.6 (77.3)
$[OxaI+H]^+$-4.1.4	67.3 (59.9)	72.5 (65.1)	76.9 (69.4)
$[OxaO+H]^+$-2.4.1	84.6 (81.5)	91.9 (88.9)	93.0 (89.9)
$[OxaO+H]^+$-2.4.2	109.2 (103.1)	117.9 (111.8)	126.2 (120.2)

[a] Calculations performed at the stated level of theory using a 6-311+G(2d,2p) basis set with geometries and vibrational frequencies calculated at B3LYP/6-311+G(d,p) level for protonation sites illustrated in Scheme 3. Gibbs energies in parentheses.

[b] Values in italics indicate energies relative to the $[AsnSer+H]^+$-1 GS including the NH_3 product.

Table 4: Fitting Parameters, 0 K Threshold Energies, and Entropies of Activation at 1000 K for Cross Sections of the Reactions Indicated[a]

TS	Frequency Scaling[b]	σ_0	n	E_0 (eV)	$\Delta S^{\dagger}_{1000}$ (J/K mol)
$TS_{O\text{-}OxaI\text{-}tet\text{-}Nc1}$	1.07	23.2 (9.0)	1.1 (0.4)	1.08 (0.09)	-83 (0.5)
$TS_{N\text{-}Fur}$	1.00			1.50 (0.13)	-0.7 (0.4)
$TS_{O\text{-}OxaI\text{-}tet\text{-}Nc1}$	1.17	31.2 (6.0)	0.7 (0.3)	1.05 (0.09)	-105 (0.7)
$TS_{N\text{-}Suc}$	1.00			1.36 (0.09)	-44 (0.5)
$TS_{O\text{-}OxaI\text{-}tet\text{-}Nc1}$	1.07	23.2 (9.0)	1.1 (0.4)	1.08 (0.09)	-83 (0.5)
$TS_{N\text{-}Fur}$	1.00			1.50 (0.13)[c]	-0.7 (0.4)
$TS_{N\text{-}Suc}$	1.00			1.36 (0.13)[c]	-44 (0.5)
$TS_{O\text{-}OxaI\text{-}tet\text{-}Nc1}$	1.00	20.4 (7.5)	1.3 (0.3)	1.14 (0.10)	-64 (0.3)
$TS_{N\text{-}Fur}$	0.93			1.54 (0.14)	21 (6)

[a] Uncertainties (reported as one standard deviation) in parentheses.

[b] Scaling factor applied to frequencies < 900 cm^{-1}.

[c] Relative threshold energies fixed to difference predicted by MP2 theory.

Table 5. 0 K Enthalpies and 298 K Enthalpies and Gibbs Energies of Reaction (in kJ/mol) for Dehydration and Deamidation Reactions of $[AsnSer+H]^{+a}$

Reaction	ΔH_0[b]	$\Delta H_{298}-\Delta H_0$[c]	ΔH_{298}	$T\Delta S_{298}$[c]	ΔG_{298}
$TS_{O\text{-}OxaI\text{-}tet\text{-}Nc1}$	104 (9)	-2.8 (0.1)	101 (9)	-15.9 (0.5)	117 (9)
		-4.6 (0.1)	*100 (9)*	*-19.5 (0.7)*	*120 (9)*
$TS_{N\text{-}Fur}$	145 (12)	3.7 (0.1)	149 (12)	-0.7 (0.2)	150 (12)
$TS_{N\text{-}Suc}$	131 (12)	0.4 (0.1)	132 (12)	-11.5 (0.1)	143 (12)

[a] Uncertainties (reported as one standard deviation) in parentheses.

[b] Experimental values from Table 4.

[c] Calculated using standard formulae and molecular constants determined at the B3LYP/6-311+G(d,p) level. Values in italics utilize the scaled frequencies used to reproduce the magnitude of the data (see Table 4).

Table 6. Comparison of 0 K Reaction Energies for the Deamidation and Dehydration Processes of $[AsnSer+H]^+$ Decomposition

Reaction	Product	Experiment[a]	B3LYP[b]	B3P86[b]	MP2(full)[b]
Deamidation	$TS_{N\text{-}Suc}$	131 (12)	151	142	130
	$TS_{N\text{-}Fur}$	145 (12)	138	145	144[c]
Dehydration	$TS_{O\text{-}OxaI\text{-}tet\text{-}Nc1}$	104 (10)	113	92	100
MAD[d]			12 (7)	8 (7)	2 (2)

[a] Experimental values from Table 4.

[b] Calculations performed at the stated level of theory using a 6-311+G(2d,2p) basis set with geometries calculated at B3LYP/6-311+G(d,p) level, ZPE corrections included.

[c] Rate-determining step is product formation rather than $TS_{N\text{-}Fur}$.

[d] Calculated mean absolute deviations (MADs) between experiment and theory for observed deamidation and dehydration reactions using all values listed.

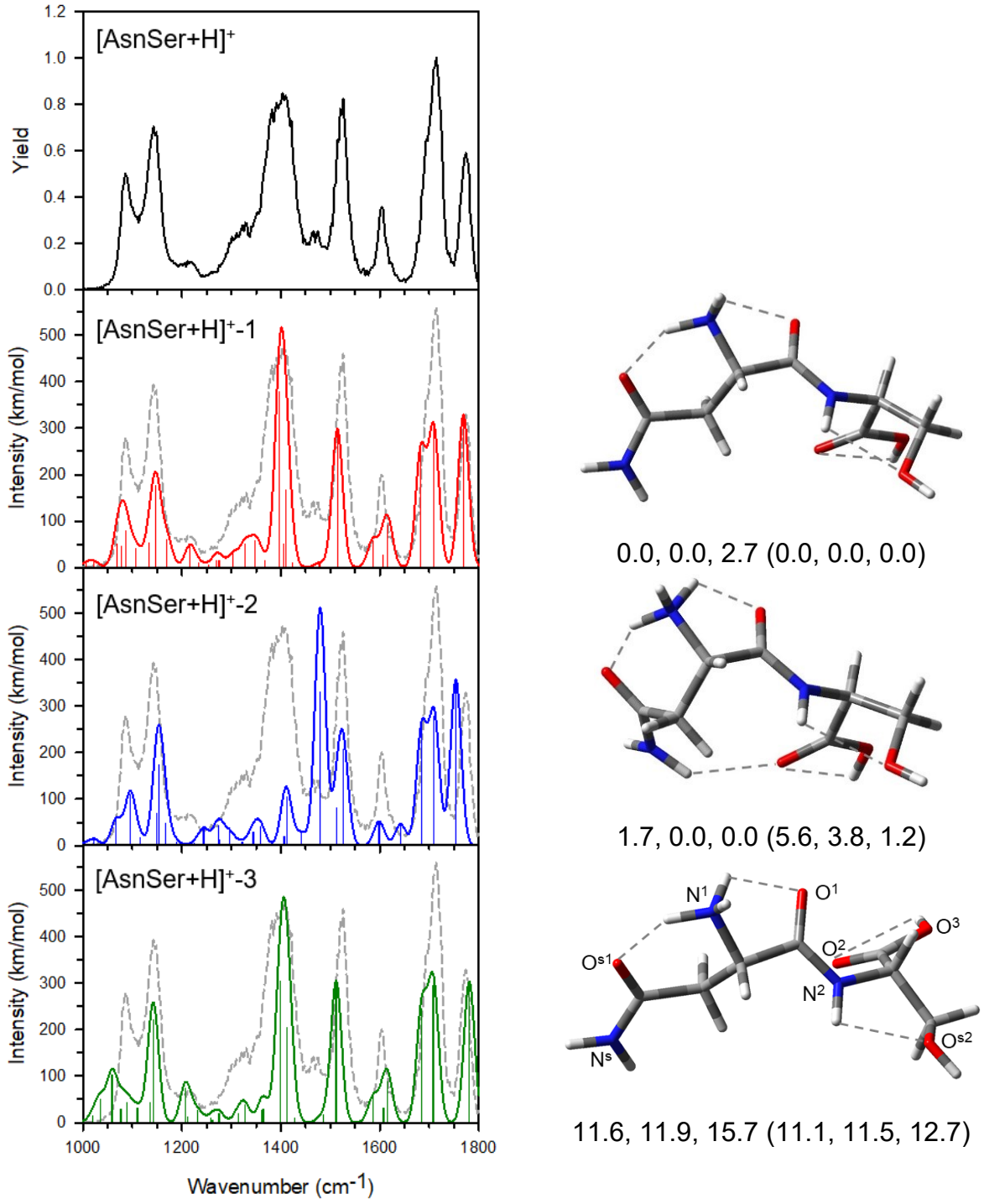

Figure 1. Experimental IRMPD spectrum of $[AsnSer+H]^+$ (black and grey traces) compared with calculated spectra for lowest energy structures (shown on the right) as calculated at the B3LYP/6-311+G(d,p) level of theory. Relative single-point Gibbs energies at 0 (298) K in kJ/mol at the B3LYP, B3P86, and MP2(full)/6-311+G(2d,2p) levels are listed. Dashed lines indicate likely hydrogen bonding interactions. Labeling of the heteroatoms is shown in the bottom right panel.

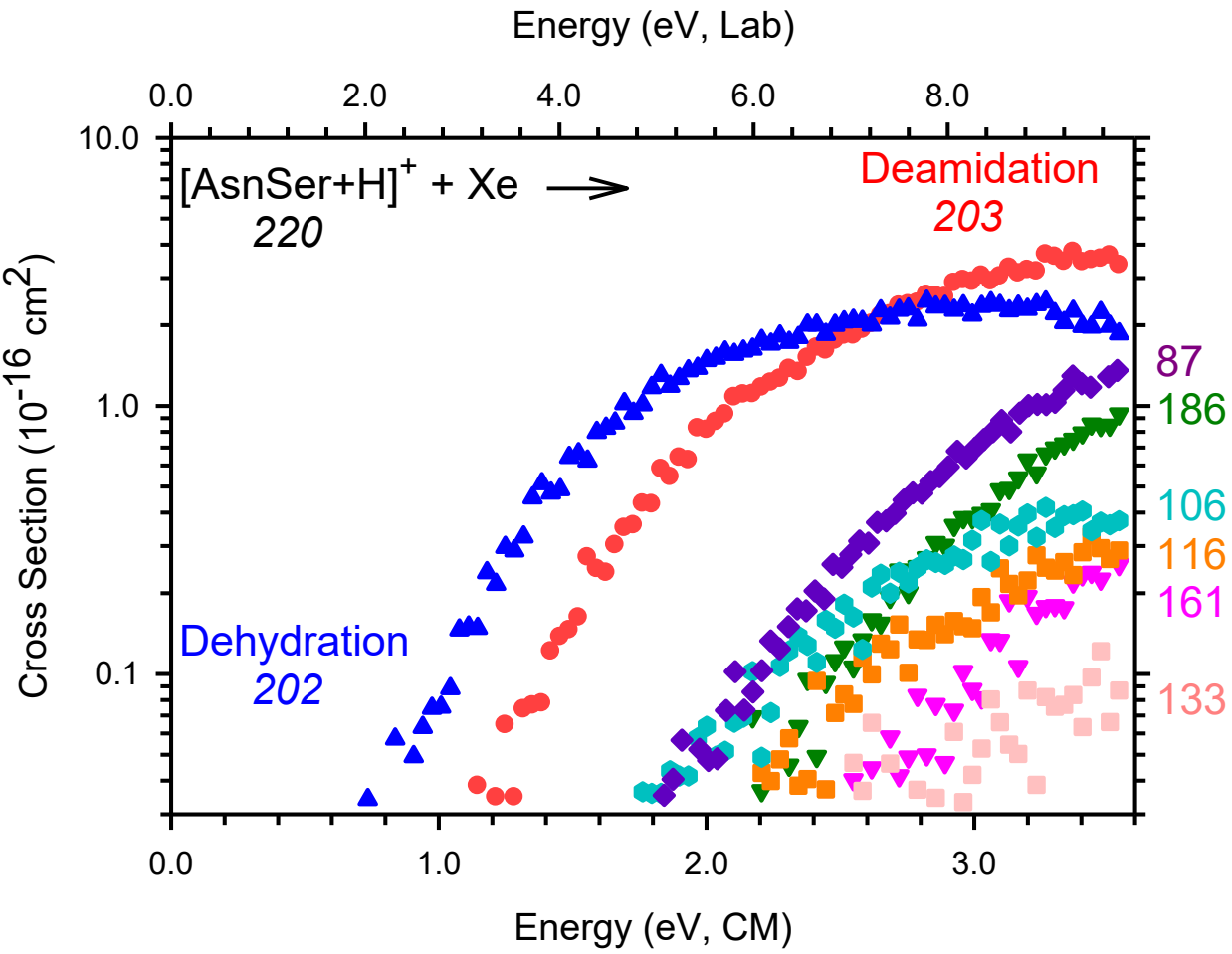

Figure 2. Cross sections for the collision-induced dissociation of $[AsnSer+H]^+$ with Xe at 0.2 mTorr as a function of kinetic energy in the center-of-mass frame (lower x-axis) and laboratory frame (upper x-axis). Numbers indicate the mass-to-charge ratio of the ionic reaction products.

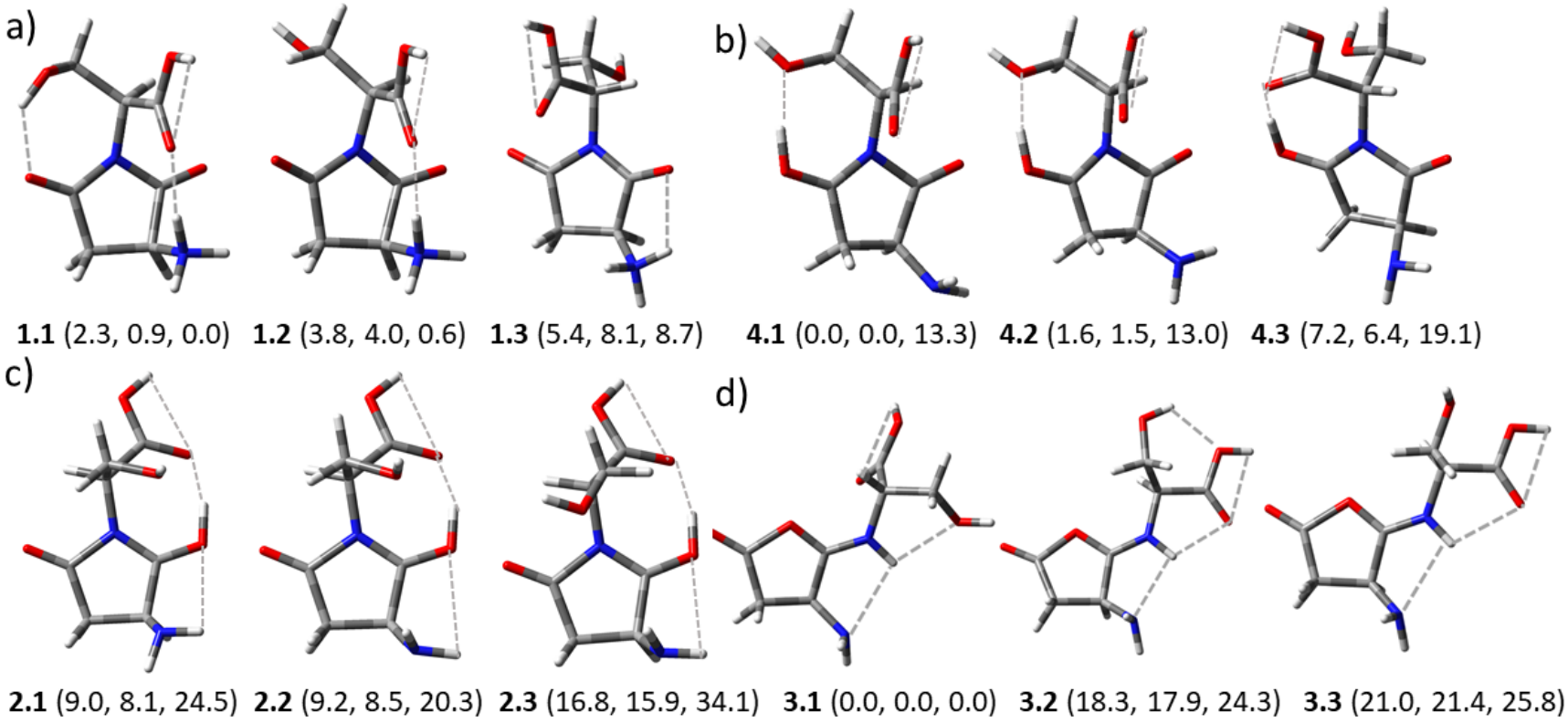

Figure 3. Select low-energy $[Suc+H]^+$ (parts a – c) and $[Fur+H]^+$ (part d) structures calculated at the B3LYP/6-311+G(d,p) level of theory. Relative single point energies at 0 K (kJ/mol) for each species calculated at the B3LYP, B3P86, and MP2(full)/6-311+G(2d,2p) levels are given in parentheses. Dashed lines indicate likely hydrogen bonding interactions.

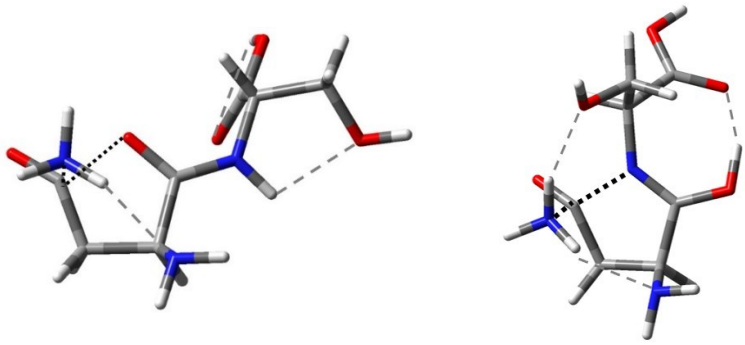

$TS_{N\text{-}Fur}$ $TS_{N\text{-}Suc}$

(***137.9***, *144.9*, 134.4) (*150.6*, ***141.7***, ***130.3***)

Figure 4. Deamidation of $[AsnSer+H]^+$. Structures calculated at the B3LYP/6-311+G(d,p) level of theory for the rate-limiting TS structures leading to furanone and succinimide formation. 0 K energies (kJ/mol) at the B3LYP, B3P86, and MP2(full)/6-311+G(2d,2p) levels of theory are given relative to the $[AsnSer+H]^+$-1 GS at each level of theory. The rate-limiting energy for each process is in italics. Bold indicates the lower energy pathway between Suc and Fur formation. Long, grey dashed lines show likely hydrogen bonding interactions. Short, black dashed lines indicate bond breaking/making interactions.

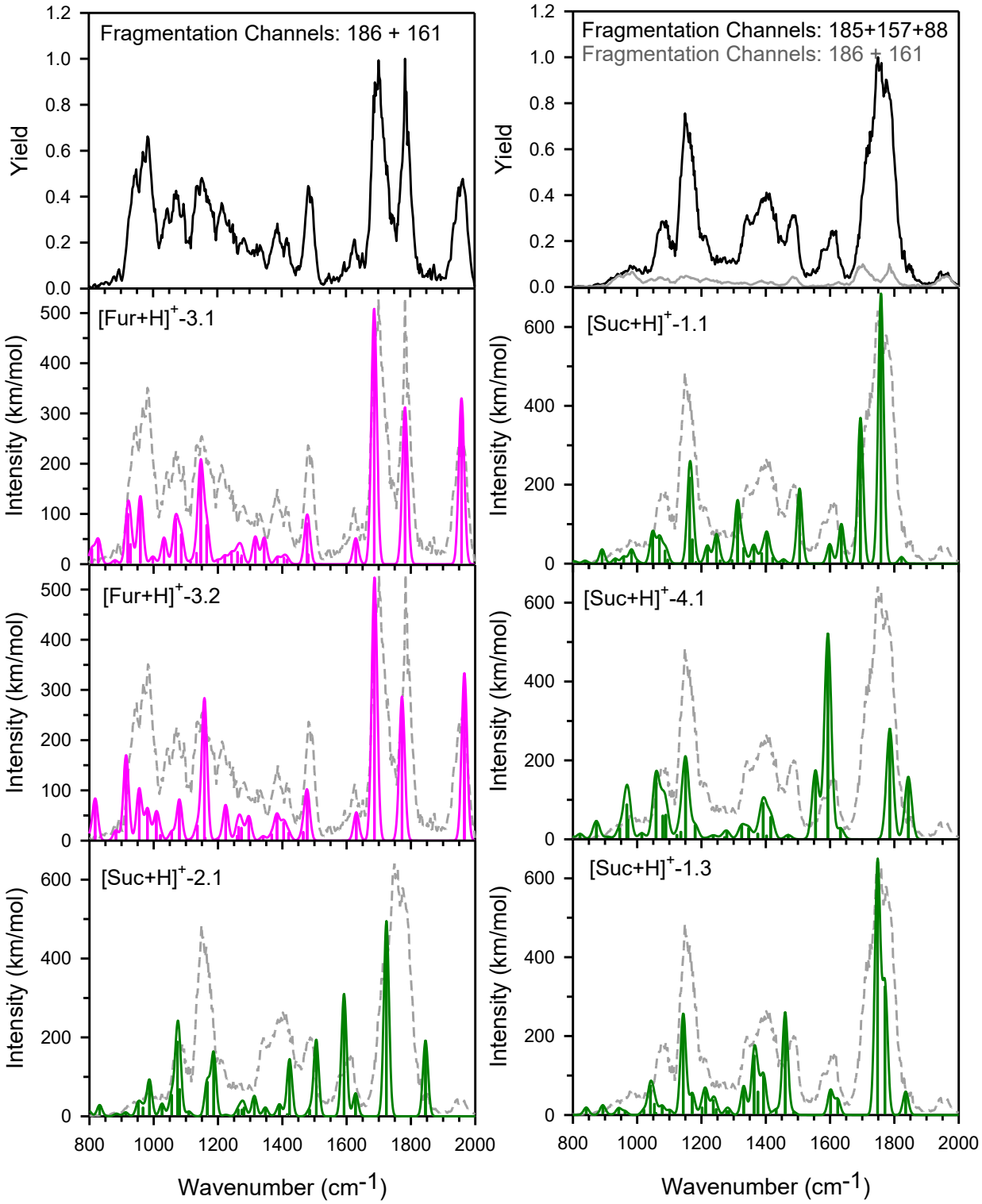

Figure 5. Experimental IRMPD spectra of $[AsnSer+H–NH_3]^+$ (black and grey) compared with the low-energy furanone structures (pink) and succinimide structures (green). The experimental spectra in the top panels are derived from the IRMPD mass channels *m/z* 186 and 161 (left and right with yield divided by 10) and those at *m/z* 185, 157 and 88 (right).

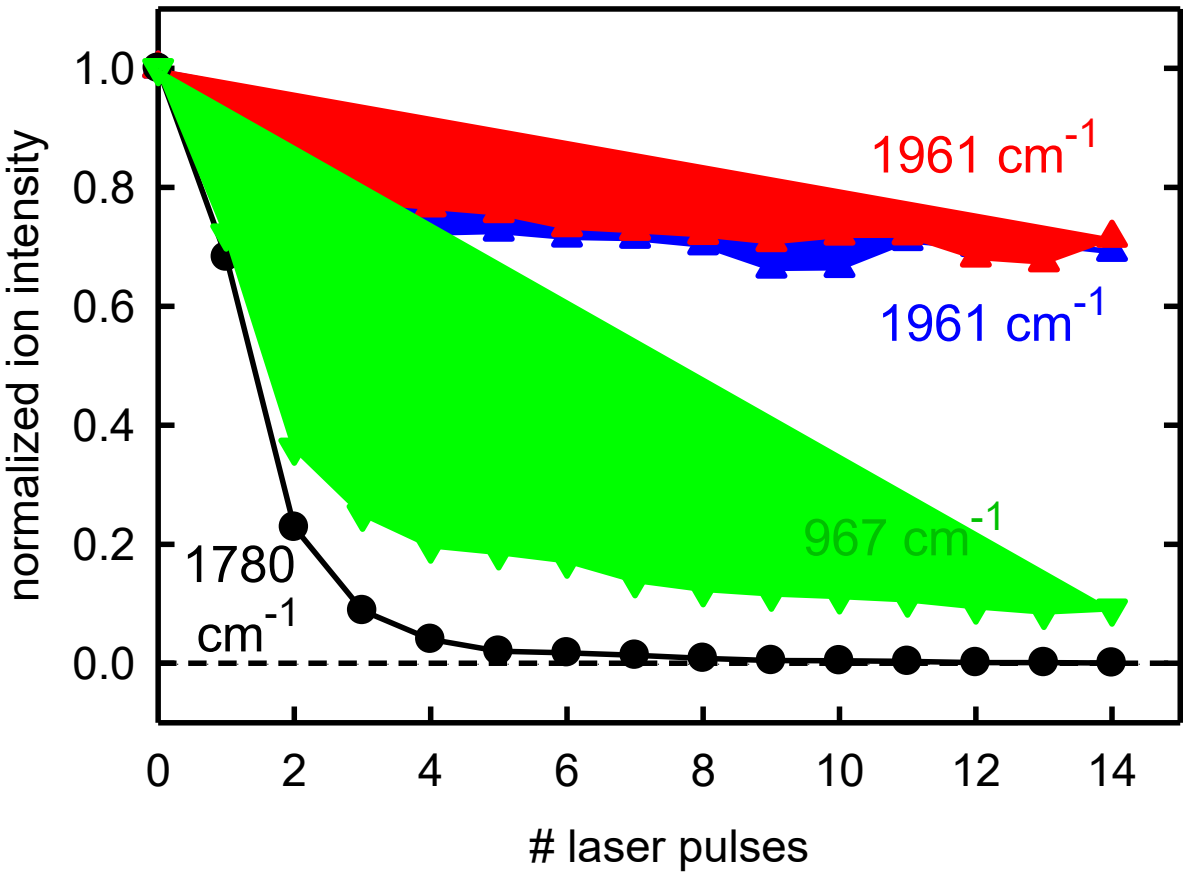

Figure 6. Irradiation of the $[AsnSer+H-NH_3]^+$ fragment (*m/z* 203) at three wavelengths: 967 cm^{-1} (green trace), 1780 cm^{-1} (black trace), and 1961 cm^{-1} (red and blue traces) as a function of the number of laser pulses. Ion intensities have been normalized to the starting population.

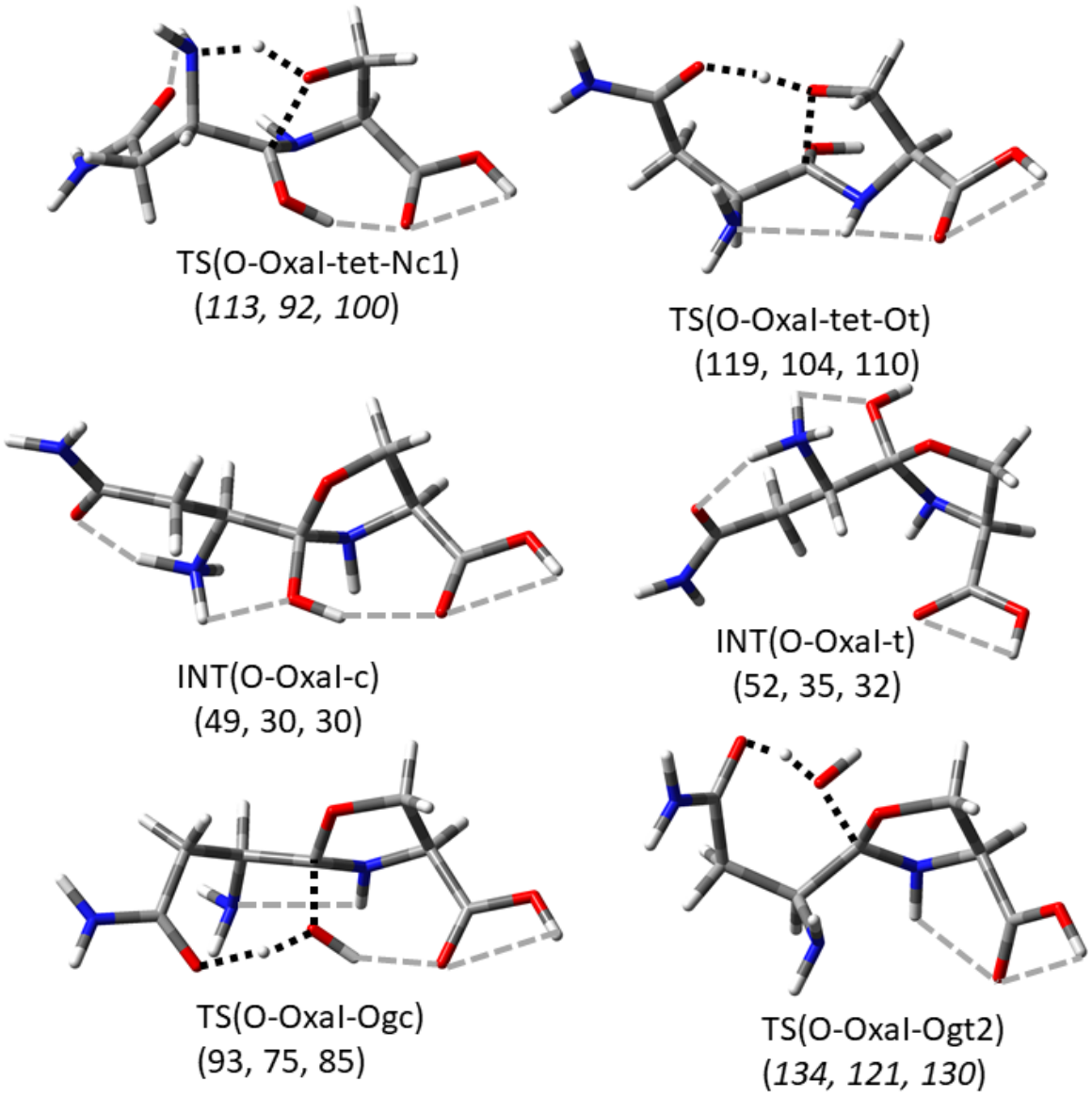

Figure 7. Dehydration of $[AsnSer+H]^+$. Structures calculated at the B3LYP/6-311+G(d,p) level of theory for the lowest energy pathways proceeding through each of two tetrahedral intermediates (INT) located along the reaction coordinate for oxazoline formation. 0 K energies (given in kJ/mol) at the B3LYP, B3P86, and MP2(full)/6-311+G(2d,2p) levels of theory are given relative to the GS at each level of theory. The rate-limiting energy for each pathway is in italics. Long, grey dashed lines show likely hydrogen bonding interactions. Short, black dashed lines indicate bond breaking/making interactions.

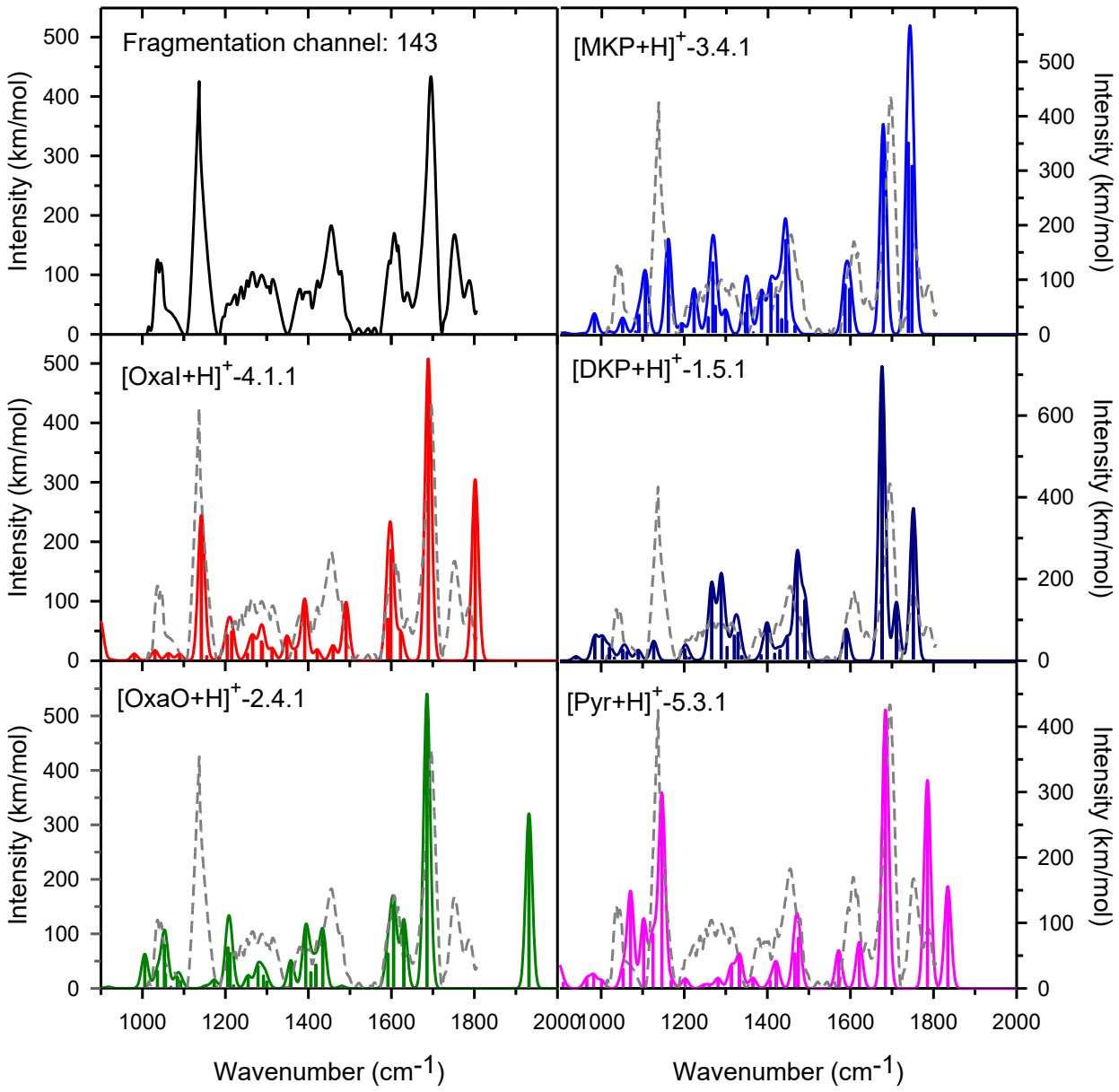

Figure 8. Experimental IRMPD spectra of $[AsnSer+H–H_2O]^+$ (black and grey) compared to calculated spectra for the lowest energy $[MKP+H]^+$, $[DKP+H]^+$, $[OxaI+H]^+$, $[OxaO+H]^+$, and $[Pyr+H]^+$ isomers. The experimental spectrum is derived from the IRMPD mass channel *m/z* 143.

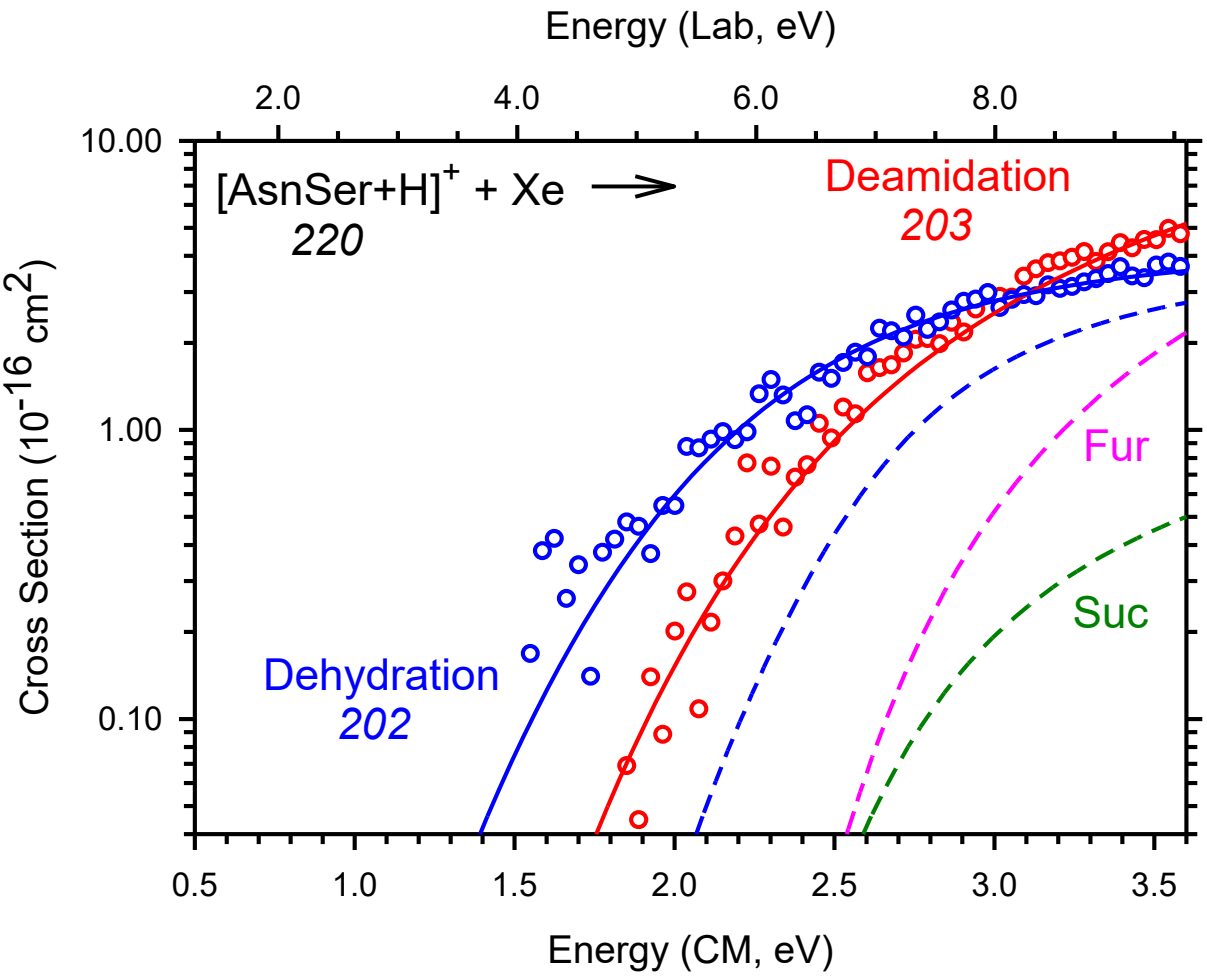

Figure 9. Cross section models of the main decomposition products of $[AsnSer+H]^+$ as a function of collision energy with Xe in the center-of-mass frame (lower x-axis) and the laboratory frame (upper x-axis). Solid lines show the best fit to the data extrapolated to zero pressure (symbols) using the model of eq 1 convoluted over the neutral and ion kinetic and internal energy distributions. Dashed lines show the model cross sections in the absence of experimental kinetic energy broadening for reactants with an internal energy of 0 K. Data were modeled assuming deamidation occurred by *both* furanone (dashed magenta) and succinimide (dashed green) formation via $TS_{N\text{-}Fur}$ and $TS_{N\text{-}Suc}$ (with relative thresholds determined by MP2 results) as well as dehydration (dashed blue) via $TS_{O\text{-}OxaI\text{-}tet\text{-}Nc1}$ using parameters listed in Table 4. Models excluding the Suc or Fur contribution look identical to those shown.

Table of Contents Graphic